Alpha Foundation for the Improvement of Mine Safety and Health

FINAL TECHNICAL REPORT

1.0 Cover Page

Grant Number: **AFC518-54**

Title: Development of an Advanced Real-Time Personal Coal Dust Monitoring Instrument Based on Photo-acoustic Spectroscopy

Organization: Board of Regents, NSHE, obo University of Nevada, Reno
1664 North Virginia Street
204 Ross Hall/Mail Stop 325
Reno, NV 89557-0240
Department of Mining and Metallurgical Engineering
University of Nevada, Reno

Principal Investigator: Dr. Karoly (Charles) Kocsis, P.Eng.
Associate Professor
Mining and Metallurgical Engineering Department
University of Nevada, Reno
E-mail: kkocsis@unr.edu
Phone: (775) 784-6989
Fax: (775) 784-4594

Co-Principal Investigator: Dr. W. Patrick Arnott,
Professor
Department of Physics
University of Nevada, Reno
E-mail: arnottw@unr.edu
Phone: 775-784-6834

Graduate Students: Apryl Witherspoon and Sarah Tesfasion
Department of Physics
University of Nevada, Reno

Reporting Period: August 01, 2017 – April 30, 2019

THIS STUDY WAS SPONSORED BY THE ALPHA FOUNDATION FOR THE IMPROVEMENT OF MINE SAFETY AND HEALTH, INC. (ALPHA FOUNDATION). THE VIEWS, OPINIONS AND RECOMMENDATIONS EXPRESSED HEREIN ARE SOLELY THOSE OF THE AUTHORS AND DO NOT IMPLY ANY ENDORSEMENT BY THE ALPHA FOUNDATION, ITS DIRECTORS AND STAFF.

Table of Contents

2.0 Executive Summary

Airborne coal and silica dust are health hazards for miners. This report demonstrates real time measurements of respirable coal and silica dust using a battery powered prototype instrument. The instrument uses photoacoustic aerosol light absorption measurements to quantify coal dust mass concentration, and aerosol light scattering measurements for quantifying total dust concentration. Silica dust concentration was obtained by subtraction of the coal dust mass concentration from the total dust concentration. Measurements were obtained at the National Institute for Occupational Safety and Health (NIOSH) Marple chamber test facility in Pittsburgh PA in August 2018. Various concentrations of coal and silica dust were introduced into the Marple chamber and total respirable dust was measured with industry standard laboratory and mine instruments based on tapered element oscillating microbalance technology. The mass concentration of respirable silica dust was measured by Fourier Transform Infrared Spectroscopy of samples collected on filters, for comparison with the prototype instrument measurements. Results indicate that the prototype instrument can be used for helping to make the mining environment a safer work place by providing real time measurements of respirable coal and silica dust. Suggested follow-on measurements and instrument development are provided.

3.0 Concept Formulation and Mission Statement:

Efforts to minimize the dangers presented by mine dust can be traced back to the first century AD, when ancient Roman mine workers wore rudimentary respirators as protection from red lead oxide dust. Nonetheless, exposure to mine dust continues to cause debilitating disease and death for thousands of mine workers every year. The NIOSH Coal Workers' Health Surveillance Program has observed an increase in black lung disease cases since 2000, with severe cases occurring in miners of younger ages (CDC 2011). This program monitors health issues among coal miners, but all miners are at risk due to exposure to silica dust and diesel particulate matter. Some mine development practices, such as slope mining and roof bolting, can expose miners to large concentrations of silica dust particles, in addition to cutting into rock strata rather than just coal seams during mining operations (Johann-Essex et al. 2017). Exposure to excessive silica levels may be responsible for the rapid progression and severity of black lung disease cases among miners (Berkes et al. 2018).

In 2014, the Mine Safety and Health Administration (MSHA) established stricter limits on respirable dust concentrations. New regulations also require the use of Continuous Personal Dust Monitors (CPDMs) to monitor concentration levels. These monitoring devices, while providing more immediate and accurate measurements than their gravimetric predecessors, only provide mass concentration measurements every 30 minutes. Additionally, CPDMs do not give insight into the composition of the dust samples (MSHA 2016). A study by the National Academies of Sciences, Engineering and Medicine concludes that monitoring dust levels to comply with MSHA regulations may not be enough to protect miners and proposes a number of additional measures. The review recommends reducing the cost of the CPDMs, as well as

developing a method to monitor silica levels in real time (NASEM 2018). Our battery-operated photoacoustic instrument offers a low-cost, portable, and accurate method for monitoring particle concentrations in real time, and its scattering and absorption measurements give insight into the presence of coal and silica dust.

Presently, the only continuous personal dust monitoring instrument in use in underground coal mines is the PDM3700 manufactured by Thermo Scientific, which is a mass-based and filter-based instrument providing near real-time dust readings. While the PDM3700 unit presents a significant step forward in assessing exposure of the mine workers to high transient/short-term dust concentrations, the unit requires further improvements due to the following shortcomings:

- Due to its filter-based technology, the PDM3700 cannot differentiate between respirable coal dust and other mineral dust particles (e.g. silica dust) collected on the filter, as well as organic material that might be present in the mine air,
- The mass-based measurement accuracy is within ±25% compared to MSHA's gravimetric measurements, which can cause inaccurate dust exposure assessments,
- Due to its tapered oscillating filter system, the unit can be easily damaged when accidentally dropped on the floor,
- The filter needs to be changed for each subsequent reading. Consequently, the unit cannot be left unattended to continually monitor dust concentration in the production workings,
- Every time the filter is changed there is a risk to break the oscillating element, which renders the unit as inoperative until the oscillating element is replaced.

This instrument may not be considered a true real-time monitoring unit, as it can only measure cumulative mass concentrations over a certain time interval.

The basic measurement principle for the prototype instrument is illustrated in Figure 1. Laser light is incident upon an aerosol particle in A). Some of the light is scattered in B). All particles regardless of composition scatter light, depending on their size, refractive index, and morphology. Aerosol in the size range most damaging to health also strongly scatter light – they have a large mass scattering efficiency (aerosol light scattering cross section divided by the aerosol mass). Some of the light is absorbed, heating the particle, B). The laser wavelength (laser light color) can be chosen so that only some particles, such as coal dust and elemental carbon in diesel exhaust, absorb light strongly. Aerosol light absorption amount depends on aerosol size, refractive index (especially the imaginary part related to light absorption), and morphology (Moosmüller et al. 2009).

The basic idea of the instrument is to use the scattering measurement to document all respirable aerosol, and to use the absorption measurement to selectively measure coal dust or the elemental carbon part of diesel particulate matter.

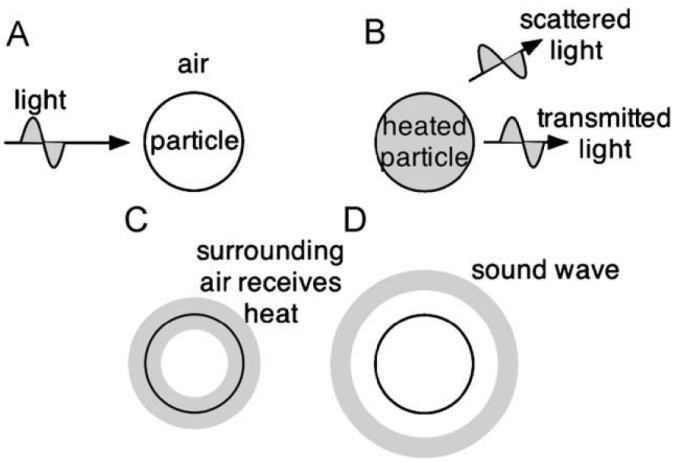

Figure 1. A light pulse is incident upon a particle (aerosol) in A). Part of the light is scattered, and part absorbed, heating the particle in B). Heat transfers from the aerosol to the surrounding air in C). Heated air expands in D), creating sound. From (Moosmüller et al. 2009).

Sensitivity to aerosol diameter can be obtained by choosing the laser light wavelength appropriately. The relationship between optical measurements and health applications will be discussed next.

Aerosol inhalation regulations are typically centered around filter-based measurements of PM1, PM2.5, PM4, and/or PM10, where for example PM2.5 refers to the mass concentration of aerosol having and a diameter less than 2.5 microns. Aerosol of different diameters are predominantly deposited in certain regions of the human respiratory system shown in Figure 2. The largest aerosol typically are deposited shortly after entrance; the smallest aerosol are close to the size of gas molecules and can diffuse to the walls of the respiratory system; 'medium'size aerosol can penetrate all the way to the alveoli where they may enter the blood stream (Hofmann 2011).

Figure 3 shows modeled total aerosol deposition in the lung as a function of aerosol diameter. Aerosol in the size range from about 0.1 microns to 2 microns can make it deepest into the lungs, where they might be absorbed in the alveoli. Figure 4 shows the fraction of aerosol deposited to a specific region if they make to that region, showing that diffusional deposition of the smallest aerosol dominates regional deposition in the alveoli region. Figure 5 shows a major complication for modeling aerosol deposition, that the warm moist lung passageways can grow hygroscopic aerosol (e.g. containing sulfur compounds) to larger size, changing their deposition dynamics.

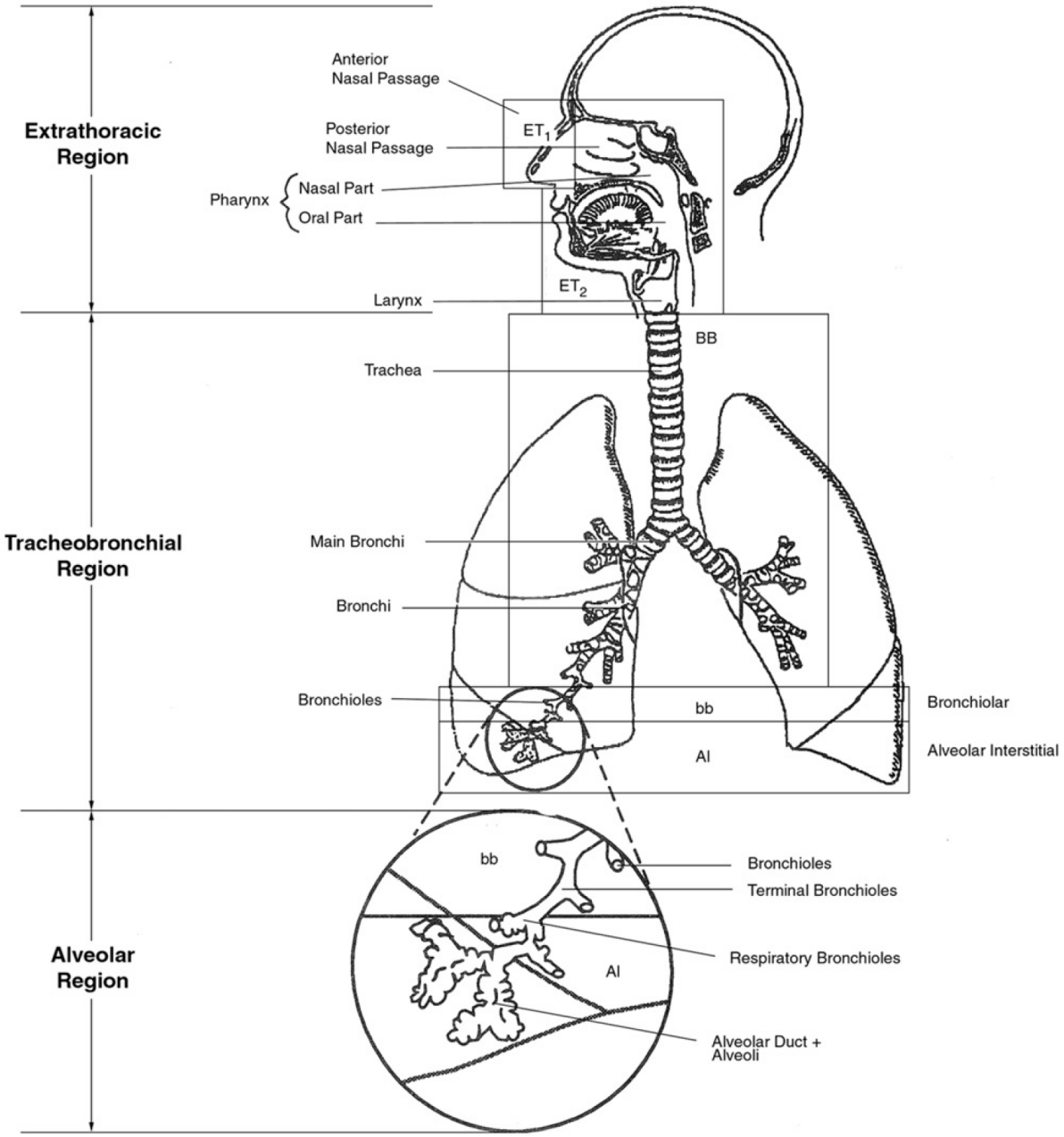

Figure 2. Human respiratory system as described for modeling aerosol deposition, from (Hofmann 2011).

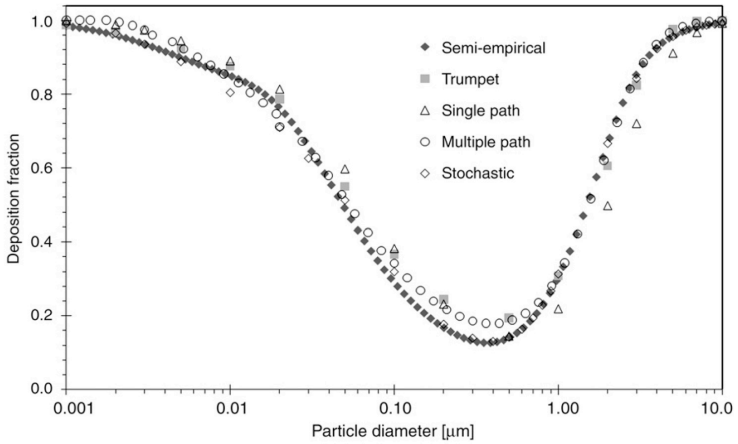

Figure 3. Model results for deposition of aerosol of unit density somewhere in the lungs for nasal sitting inhalation. From (Hofmann 2011).

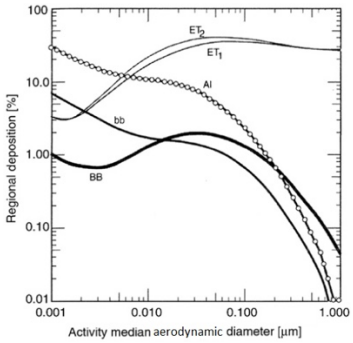

Figure 4. Model results for regional aerosol deposition. AI is the alveoli region. For example, 2% of the aerosol of 0.1-micron diameter are deposited in the AI. From (Hofmann 2011).

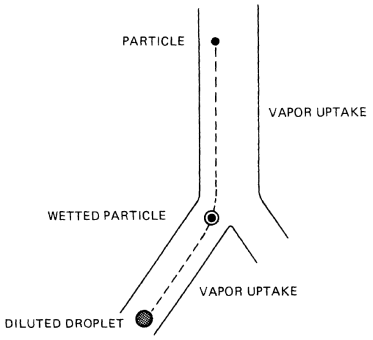

Figure 5. An aerosol particle enters a warm moist lung passageway at the top. Hygroscopic aerosol may uptake water vapor and grow to larger diameter, changing deposition dynamics. From (Martonen et al. 1985).

Recent investigations have demonstrated the usefulness of optical methods for measuring coal and silicate dust. Laboratory measurements have demonstrated the usefulness of photoacoustic measurements of aerosol light absorption for quantifying coal dust (Ajtai et al. 2011). Real time measurements of light scattering as a proxy for aerosol mass concentration for quartz and fly ash aerosol have been demonstrated and optimized (Chen et al. 2018).

Measurements of coal complex refractive indices are available for modeling light scattering and absorption by these aerosol (McCartney; Ergun 1962).

A perfect aerosol mass measurement has the same sensitivity regardless of aerosol size. Filter based measurements are approximately 'perfect' in this sense. Model results for quartz dust aerosol light scattering as a proxy for aerosol mass measurement is illustrated in Figure 6 for the laser wavelength used in the prototype instrument. The y-axis shows aerosol scattering cross section divided by aerosol mass for single particles. In a perfect instrument for mass measurement by light scattering these curves would be a flat light. The red curve illustrates sensitivity to aerosol mass in a diameter range from about 0.1 microns to 10 microns, with peak sensitivity at around 0.7 microns. Therefore, it will always be necessary to empirically calibrate scattering measurements to a site-specific location where aerosol tends to have a similar size distribution. However, in a different sense the scattering peak in Figure 6 is well suited to be most sensitive to aerosol in the size range where they reach deepest into the lungs as shown Figure 3. The peak in Figure 6 moves to the right (left) for longer (shorter) wavelength radiation so that sensitivity for specific aerosol size ranges can be obtained by laser wavelength choice. Multiple wavelength instruments can allow for measuring aerosol size (Lewis et al. 2008).

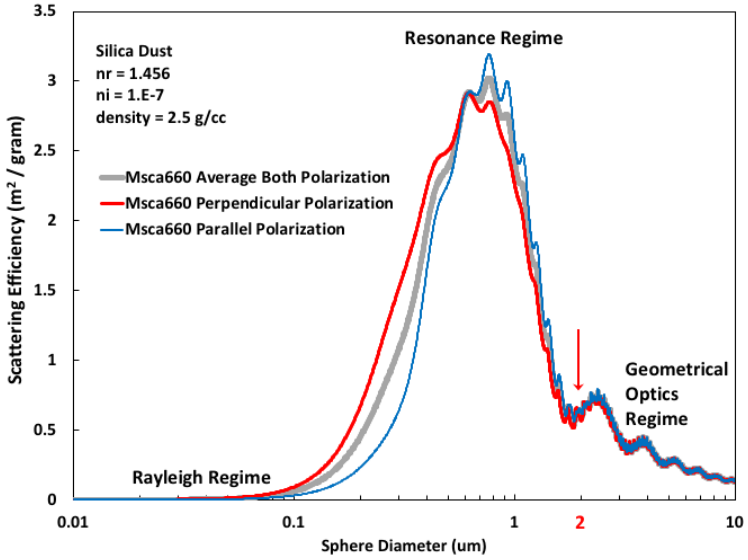

Figure 6. Modeled (with Mie theory) mass scattering efficiency for silica dust as a function of sphere diameter for laser beam polarization parallel and perpendicular to the scattering plane. The prototype instrument uses perpendicular polarization (red curve). Absorption efficiency (not shown) is negligible for silica dust for 660 nm wavelength.

Figure 7 and Figure 8 show the mass scattering and absorption efficiency, respectively, for coal dust for different types of coal. The scattering sensitivity range is like that of silica dust shown in Figure 6. Note that the mass absorption efficiency curve in Figure 8 does have a flat region where the mass weighted absorption measurement is independent of aerosol size. This flat region is the motivation for optical measurement of aerosol black carbon mass concentration instruments, useful especially for diesel particulate matter aerosol.

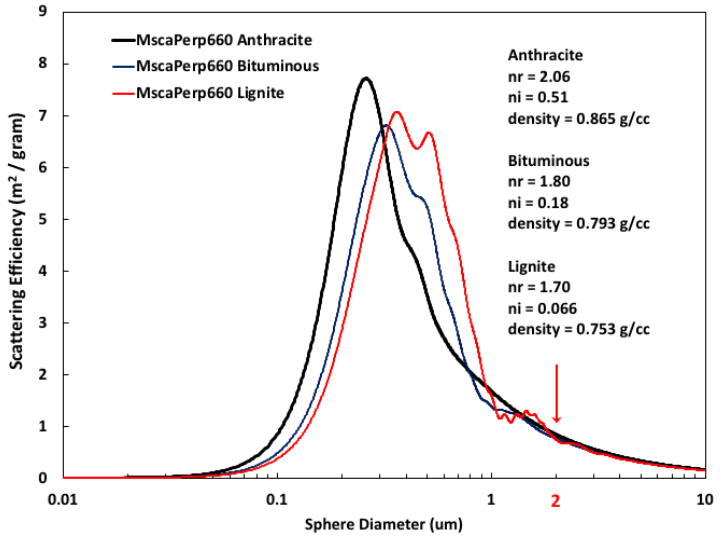

Figure 7. Modeled (with Mie theory) mass scattering efficiency for coal dust as a function of sphere diameter for laser wavelength 660 nm and perpendicular polarization state for different types of coal.

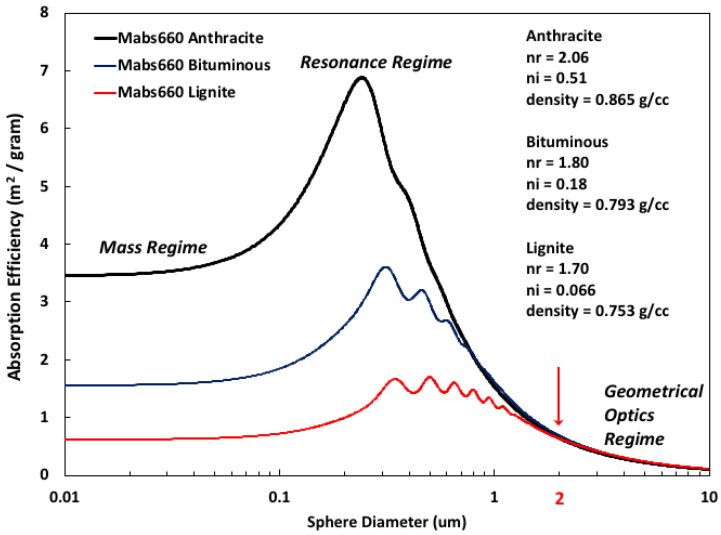

Figure 8. Modeled (with Mie theory) mass absorption efficiency for coal dust as a function of sphere diameter for laser wavelength 660 nm and perpendicular polarization state for different types of coal. In the mass regime aerosol light absorption does depend on aerosol volume making this regime approach an ideal mass monitor. Elemental carbon aerosol in diesel particulate matter is closest to Anthracite in its optical behavior for light absorption. Note that in the geometrical optics regime absorption efficiency does not depend on aerosol type.

In summary, optical measurements at 660 nm as a proxy for aerosol mass concentration have size sensitivity that overlaps well with the aerosol lung penetration to the alveoli region illustrated by the minimum in the curve of Figure 3. Our optical measurements are calibrated to obtain true absorption and scattering coefficients (Lewis et al. 2008). Use of optical measurements as a proxy for aerosol mass concentration is best carried out with site specific calibration to typical aerosol size and composition as described for vehicle emissions

(Moosmuller et al. 2001a, 2001b), and for mine measurements (Lebecki et al. 2016). Once specific calibration is obtained, optical measurements are very quick (1 second), and very sensitive (1 microgram/m^3). *It should be noted that for aerosol of diameter 2 microns, important for dust mass concentration, that Figure 6, Figure 7, and Figure 8 show that the we are in the geometrical optics regime where sensitivity to aerosol composition and size is greatly reduced compared with smaller diameters, thus making our choice of 660 nm quite useful.*

Light scattering measurements with compact instruments such as the TSI model 3330 (TSI 2019) are often used to quantify possible aerosol exposures (Maragkidou et al. 2018). Portable instruments based on the filter method have been developed to measure aerosol light absorption in general (Aethlabs 2019) and in the mining environment (Noll et al. 2013) especially for measuring the elemental carbon component of diesel particulate matter. Filter based measurements of light absorption require frequent operator intervention to replace the filter, and the data must be interpreted carefully due to aerosol filter loading effects (Arnott et al. 2005). A portable dust monitor (model PDM3700) based on gravimetric measurements and the tapered element oscillating microbalance technology is available (ThermoScientific 2019a) . A recent article comparing respirable (PM4) light scattering pDR-1500 (ThermoScientific 2019b) and PDM3700 mass concentration measurements for a variety of aerosol types with a reference filter method found that the PDM3700 was adequate for all samples except coal dust while the light scattering based instrument response substantially varied with aerosol refractive index and therefore aerosol type (Halterman et al. 2018). Using a PM1 inlet, real time photoacoustic and Dusttrak measurements of the elemental and total carbon content of diesel particulate matter was demonstrated for a working gold mine (Arnott et al. 2008).

The following summarizes the current state of the science and engineering with regard to personal exposure measurements of respirable aerosol mass concentration in the mining environment.

- The PDM3700 portable dust monitor based on the tapered element oscillating microbalance technology generally achieves adequate precision with 30 minute time averaged samples and is accurate for most aerosol types.
- Optical light scattering measurements as a proxy for aerosol mass such as the pDR-1500 have excellent precision after a few seconds time average, though accuracy depends on aerosol refractive index and therefore site specific calibration is necessary.
- Aerosol light absorption measurements define the black carbon mass concentration and therefore by definition are useful for this measurement. In all instruments it is usual to control the relative humidity to be below about 60% so that dry aerosol mass is measured.
- Optical light scattering measurements of respirable PM and in situ black carbon mass concentration may be useful for long term unattended operation for ventilation on demand-based control systems and underground monitoring whereas filter based methods are mostly impractical as a result of too much operator intervention.

The prototype portable instrument described here uses the in situ photoacoustic method for black carbon mass concentration relevant to coal dust and the elemental carbon component of diesel particulate matter and aerosol light scattering for total respirable dust

measurements, with aim to using it as both a personal sample and as an unattended long term mine air quality monitor.

This report is organized to include sections on measurement methods; coal and mineral dust aerosol generation; real time measurements that compare laboratory standard and prototype instrument results; and appendices to further document the prototype instrument. Readers especially interested in comparing the measurements obtained from conventional and prototype instruments can view Figure 15 and Figure 16 to understand the calibration and measurement procedures; measurement results are shown in Figure 26 and Figure 27.

4.0 Proof-of-Concept Technology Components:

Our aim is a practical, portable instrument for real time use in mines. The prototype instrument measurement method, illustrated in Figure 9 and Figure 10, is based on aerosol light absorption measurements by the photoacoustic method (Arnott et al. 1999) and light scattering measurements by the reciprocal nephelometer method (Abu-Rahmah et al. 2006; Lewis et al. 2008).

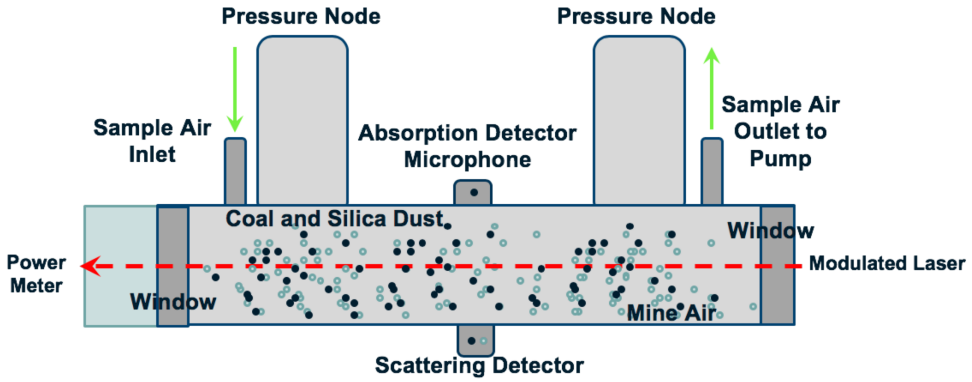

Figure 9. Schematic of the optical instrument for measuring coal and silica dust. Mine air contains both silicate and coal dust, open blue and closed black circles, respectively. The laser beam polarization is perpendicular to the plane of the figure. A 660 nm laser is used.

The laser beam wavelength is 660 nm to provide good sensitivity to typical respirable dust and, practically speaking, because reliable diode lasers are readily available. The modulated laser power is typically 60 mW. The laser beam polarization is perpendicular to the plane of the figure in Figure 9 to increase the sensitivity to smaller aerosol as shown in Figure 6. Coal and silica dust both scatter light while light absorption is predominantly from coal dust. The instrument measures aerosol light absorption and scattering coefficients, β_{abs} and β_{sca}, with dimensions of Mm^{-1}. Note that 1 Mm is 10^6 meters. These coefficients are the concentration of light absorption and light scattering and are related to the aerosol size distribution by (Moosmüller et al. 2009)

$$\beta_{abs} = \int_0^\infty \rho \frac{dV}{dD} AE \, dD \approx \boldsymbol{CoalDustPM4} * AE \quad , \tag{1}$$

$$\beta_{sca} = \int_0^\infty \rho \frac{dV}{dD} SE \, dD \approx \boldsymbol{TotalDustPM4} * SE \, , \tag{2}$$

where ρ is the aerosol density; *dV/dD* is the aerosol volume distribution function; *AE* and *SE* are the aerosol absorption and scattering shown in Figure 6, Figure 7, and Figure 8 as a function of aerosol diameter; and ***CoalDustPM4*** and ***TotalDustPM4*** are the desired mass concentration of coal and total dust of aerosol below 4 micron diameter obtained with use of a cyclone before the instrument inlet. Instrument calibration amounts to obtaining appropriate values of *AE* and *SE*; values will be reported in the demonstration section of this report.

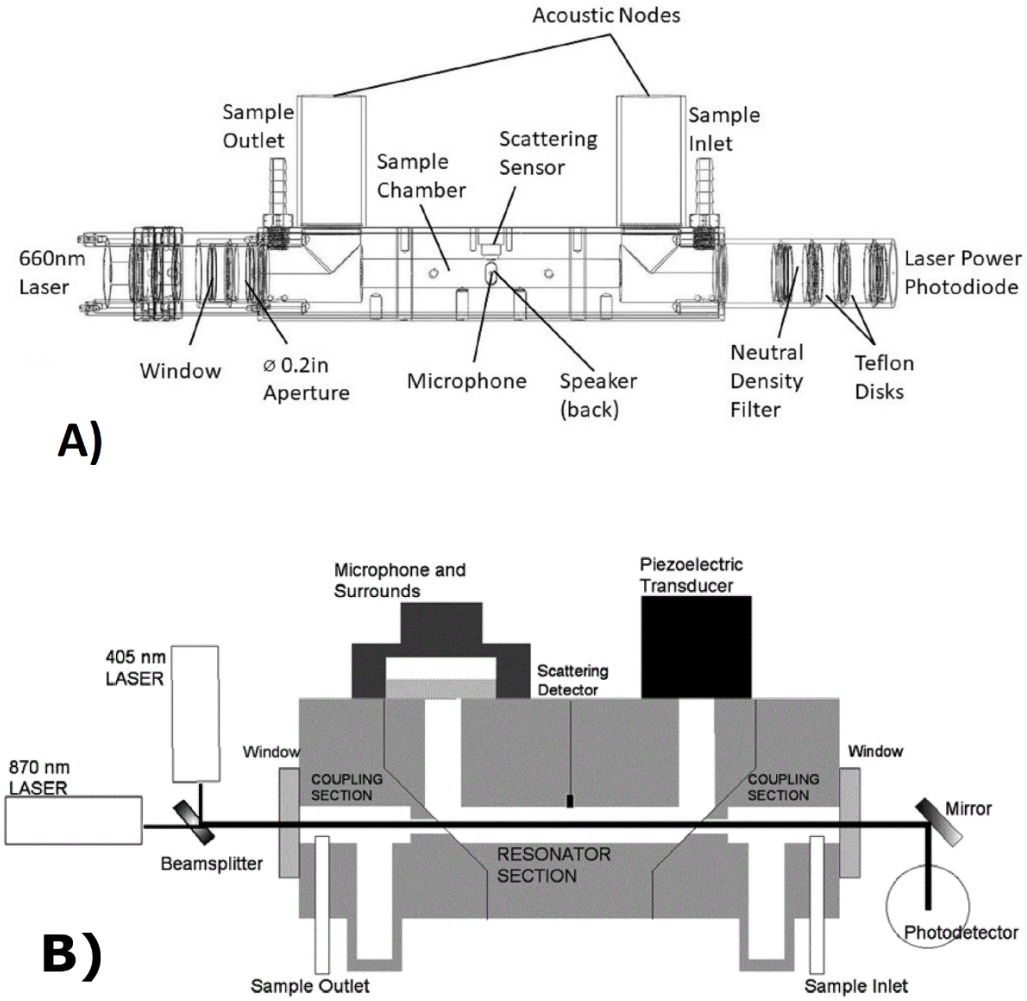

Figure 10. A) Relative scale drawing of the current prototype instrument, and B), of previous instrument (Lewis et al. 2008). In A) the sample chamber is the acoustic resonator. In A) a hearing aid speaker and microphone is used for absorption measurements, and a photodiode for scattering, while in B) an expensive 1" diameter microphone is used and a photomultiplier tube is used for scattering detection. B) illustrates dual laser wavelength operation. Side branches labeled acoustic nodes act as ¼ wavelength oscillators that band stop noise from the sample inlet and outlet. Manufacturing costs of the basic resonator in A) are a factor of 15 lower than in B). A) resonates at around 1367 Hz while B) is around 1500 Hz.

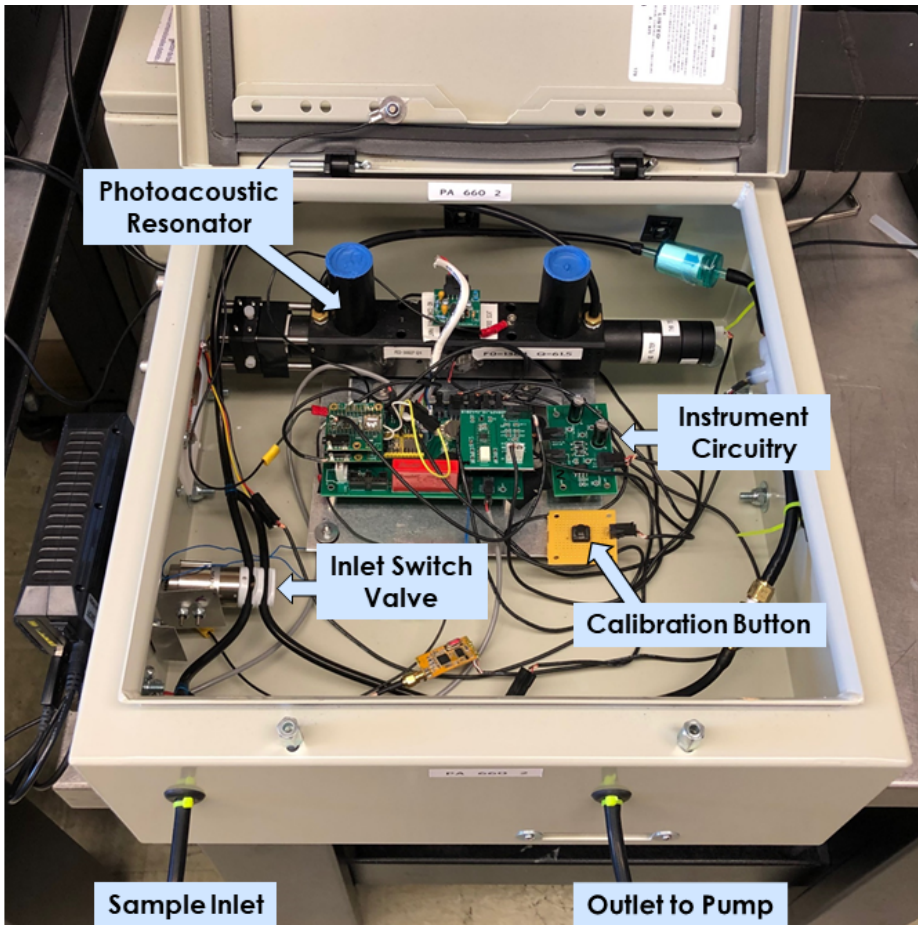

Figure 11. Photograph of the inside of the current prototype instrument. The photoacoustic resonator, printed circuit board, inlet switch valve, and plumbing are mounted inside a steel enclosure for protection against the elements and electrical noise.

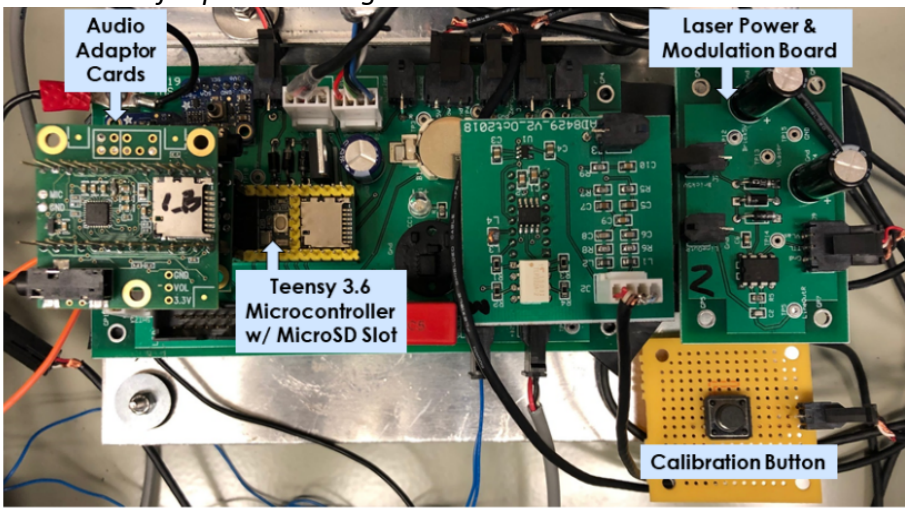

Figure 12. Photograph of the circuitry which operates the prototype instrument. A Teensy 3.6 microcontroller and two PJRC Audio Adaptor Boards are used for inputting and outputting signals and for processing data.

Figure 13. Photograph of the side of the prototype instrument enclosure. A screen is mounted to allow for monitoring of instrument operations. The power supply is mounted on the outside for easy replacement. The radio antenna transmits collected data serially.

Figure 11, Figure 12, and Figure 13 show the instrument prototype. Most of the instrument components are mounted inside a NEMA Type 12 enclosure, which provides protection against circulating dust and exposure to water. The enclosure is electrically grounded to inhibit electrical interference from the environment. On the printed circuit board, a Teensy 3.6 microcontroller and two PJRC Audio Adaptor Boards are used to conduct instrument operations, as described in Appendix 2. Microcontroller-Based Photoacoustic Instrument Description. An LCD screen displays current processes and measurements so that users can monitor instrument activity.

The main laboratory instrument for comparison purposes is the TEOM 1400. It is based on the use of a tapered element oscillating microbalance measurement of a PM filter placed on the end of hollow tube (Patashnick; Rupprecht 1991). A schematic of the TEOM is shown in Figure 14. Measurements from the portable personal dust monitor (PDM) sampler version of

the TEOM used in the mining industry (Gillies; Wu 2006) will also be used in this report. The PDM recently underwent a change of its inlet system to a lapel style inlet (Mischler et al. 2019).

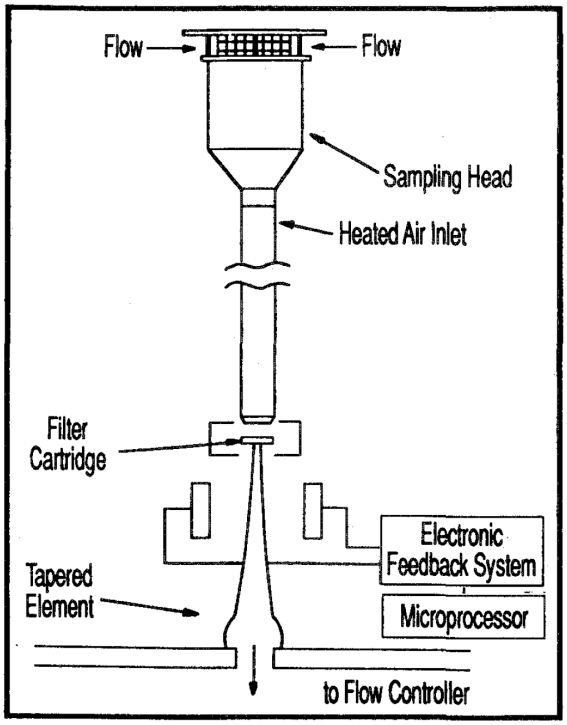

Figure 14. Illustration of the tapered element oscillating microbalance (TEOM) instrument. From (Patashnick; Rupprecht 1991). The tapered element and filter cartridge form a spring-mass system whose resonant frequency depends on the amount of aerosol mass loaded on the filter.

5.0 Proof of Concept Evaluation:

The calibration and measurement procedures are discussed first.

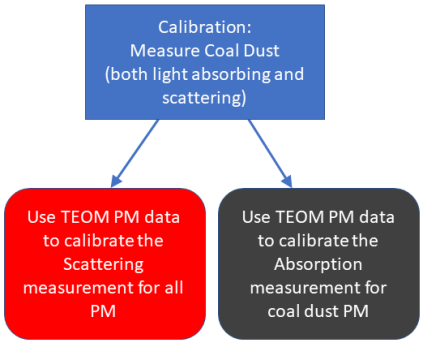

Figure 15. Calibration of the prototype instrument for total PM and coal dust concentration measurements. Coal dust both scatters and absorbs radiation at the 660 nm wavelength of the prototype instrument.

Figure 15 shows the procedure used for calibrating the prototype instrument for total PM and coal dust concentration measurements. Coal dust both absorbs and scatters light;

therefore, the scattering measurement can be calibrated for total PM. The absorption measurement is calibrated for coal dust concentration measurement.

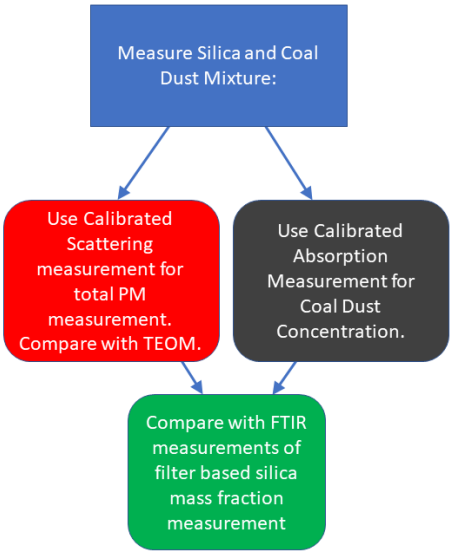

Figure 16. Measurement and evaluation procedures for comparing results from the prototype instrument with more standard laboratory methods.

Figure 16 shows the procedure used to evaluate the prototype instrument measurements. Total PM is measured by both the TEOM and the light scattering detector of the prototype instrument. Coal dust is measured with the light absorption detector, and total silica fraction is compared with that derived from the prototype instrument measurements.

Testing was performed at the Pittsburgh National Institute for Occupational Safety and Health (NIOSH) laboratory using one of the Marple chambers (Marple; Rubow 1983), see Figure 17. Aerosol are dispersed and delivered to the interior of the chamber using a TSI Model 3400 Fluidized Bed Aerosol Generator. The 5 PDM instruments were located inside the chamber and were operated by battery. The TEOM and prototype instrument were located external to the

chamber. All instruments had cyclones for passing PM4. The prototype instrument used a URG cyclone with a flow rate of around 2 LPM to achieve a 4 micron cut point, see Figure 18.

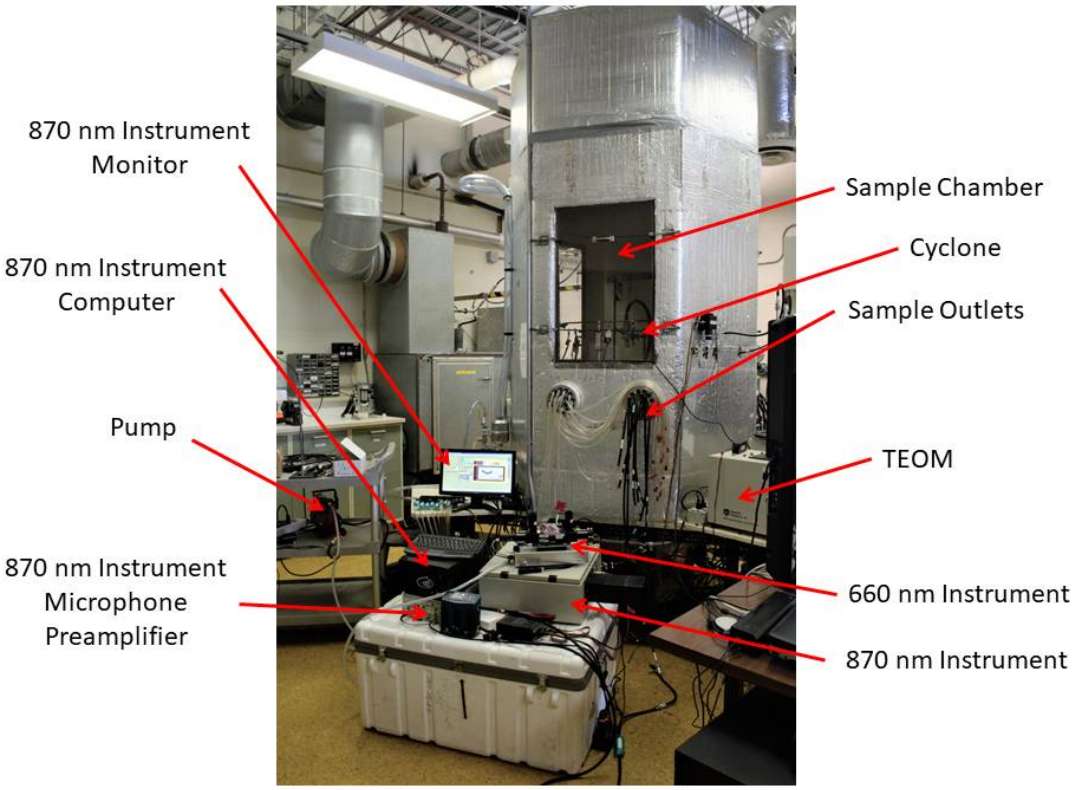

Figure 17. "Marple" chamber for testing instruments for aerosol measurements. The prototype instrument and a previous version operating at 870 nm are shown in the foreground. Personal dust monitors were inside the chamber.

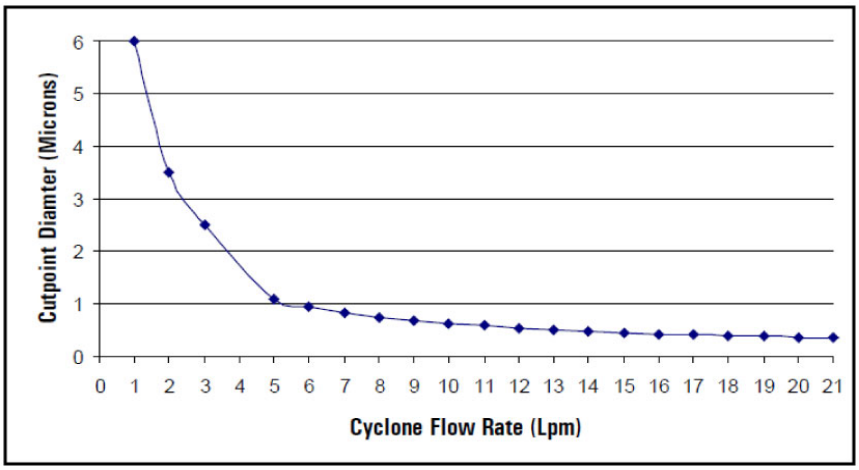

Figure 18. Characteristics of the URG-2000-30ED cyclone used for the prototype instrument.

The first two tests used 100% coal dust at low relative humidity (RH) and high RH to achieve calibration as indicated in Figure 15. The final test had nominally 25% silica 75% coal dust at low relative humidity for evaluating the prototype instrument ability to separately measure coal and silica dust as indicated in Figure 16. Each test included reaching 4 different

concentration plateaus of 2.5, 1.5, 0.75, and 0.25mg/m^3 for 40-minute periods. These tests were performed on three separate days due to the lengthy duration of each test and due to the required differences in aerosol and relative humidity within the testing chamber. The differences in relative humidity were incorporated to test the prototype instrument's performance in conditions that resemble those of the mining environment.

This testing was performed using the two photoacoustic instruments of wavelengths 660 nm and 870 nm, one continuous ambient particulate monitor referred to as TEOM (tapered element oscillating microbalance), four gravimetric samplers, and four particulate dust monitors (PDMs). The gravimetric samplers and PDMs were situated inside the testing chamber at four different locations. Exterior tubing was used to draw the sample aerosol into the two photoacoustic instruments and the TEOM, which were located outside of the testing chamber. The data collected from the TEOM acts as a reference which we can use to calibrate the 870 and 660 nm instruments and measure their performance. The sample dust of either 100% coal dust or 25% silica and 75% coal dust was thoroughly mixed and sent into the testing chamber using a fluidized bed aerosol generator. Once the aerosol entered the testing chamber, it was passed through the URG-2000-30ED cyclone. The cyclone ensures that particles smaller than a given diameter are passed through the photoacoustic instrument, while most of the larger particles are deposited into the cyclone bottom.

100% Coal Dust Low RH Test

This first test performed at the NIOSH facility involved generating an aerosol composed of 100% coal dust and passing it through the testing chamber shown in Figure 17. The relative humidity inside the testing chamber was adjusted to a low value of 25% during this test.

Electron microscopy filters were introduced into the sample inlet system to collect aerosol in addition to collecting data for sample aerosol mass concentration, absorption, and scattering. These polycarbonate 100 nm nuclepore filters can be analyzed with a scanning electron microscope (SEM) to determine the size distribution, morphology, and elemental composition of the particles. During this test, 3 electron microscopy filters were used with different exposure times determined by the scattering concentration time of filter insertion. Two of the electron microscopy filters were exposed to aerosol for 10 minutes, while the third filter was exposed for 5 minutes.

To determine the effect of differing particles sizes on the absorption and scattering coefficients measured by both photoacoustic instruments, we alternated between using both the 660 nm and 870 nm instruments and using the 660 nm instrument alone to collect data during each 40-minute concentration plateau. This was possible because the flow rate through the URG cyclone varied between the two configurations, causing the particle size cutoff to change between each case. In the first case, the flow rate was 2.2 lpm with both instruments, corresponding to a particle size cutoff of approximately 3.2 µm as shown in Figure 18. In the second case with only the 660 nm instrument, the flow rate was adjusted to 1.7 lpm with a needle valve. This corresponds to a particle cutoff of approximately 4 µm to match the cyclone cutoff of the TEOM.

Figure 19 is a scatterplot of TEOM mass concentration with respect to absorption and scattering coefficients for the 660 nm instrument. Since coal dust was the only aerosol in the system, we can assume all absorption and scattering was caused by the coal dust and calibrate our absorption and scattering mass concentration values to the TEOM values for the procedure illustrated in Figure 15. Performing a linear fit to this data resulted in calibration factors for the 660 nm instrument of 1.73 (micrograms/cubic meter)/Mm^{-1} for scattering measurements and 1.53 (micrograms/cubic meter)/Mm^{-1} for absorption measurements. These calibration factors are equivalent to the inverse of the mass scattering (M_{sca}) and mass absorption efficiencies (M_{abs}), resulting in values of 0.578 (m^2/gram) for M_{sca} and 0.654 (m^2/gram) for M_{abs}. Size dependent theoretical mass scattering (Figure 7) and absorption efficiencies (Figure 8) can be used to estimate the diameters of particles that were present during testing. These mass efficiencies cross the theoretical curves at about an aerosol diameter of 2 microns.

The TEOM and 660 nm optical data are highly correlated, as shown by the high R^2values of about 0.97 for both scattering and absorption data in Figure 19. The absorption and scattering data recorded by the 660 nm instrument would most likely have resulted in a higher correlation with the TEOM data if the periodic changes to the inlet system to remove and add the 870 nm instrument during each of the 40-minute concentration plateaus had not been performed. Sudden movement and changes within the inlet system introduced uncertainty to the 660 nm data either due to pressure changes or due to the inlet system's exposure to noise from outside the testing chamber.

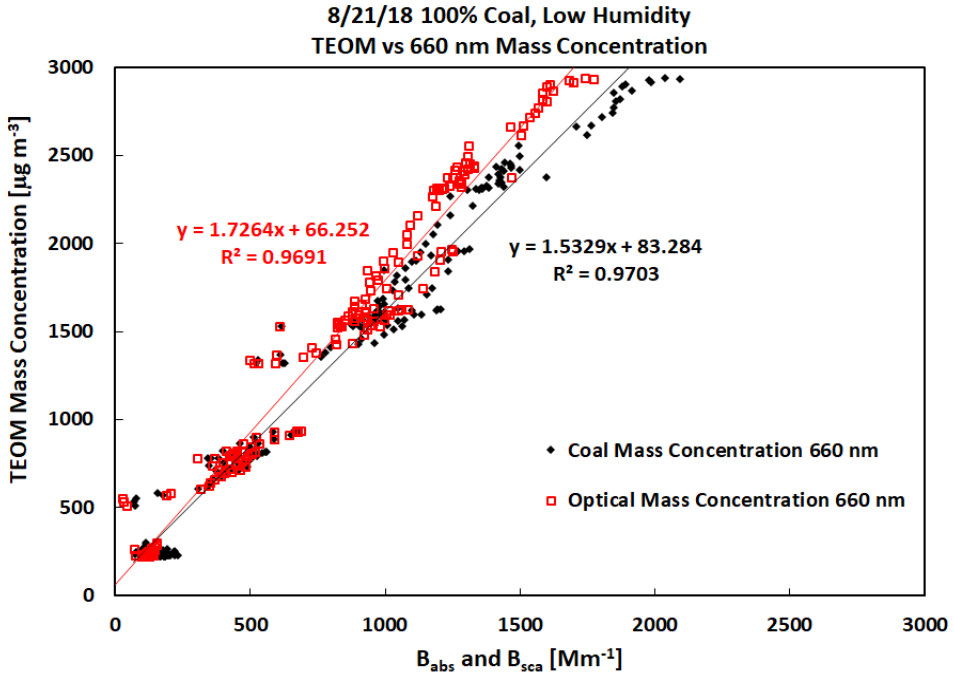

Figure 19. Scatter plot of TEOM mass concentration and aerosol scattering and absorption measurements for coal dust for low relative humidity.

Figure 20 is a time series of the absorption (coal mass) and scattering (optical mass) data from the 660

instrument along with the TEOM data achieved after multiplying the aerosol light scattering and absorption measurements by the slopes of the curves in the scatter plots of Figure 19. The data from the 660 nm instrument was time aligned with the TEOM data to account for differences in time recording between the instruments.

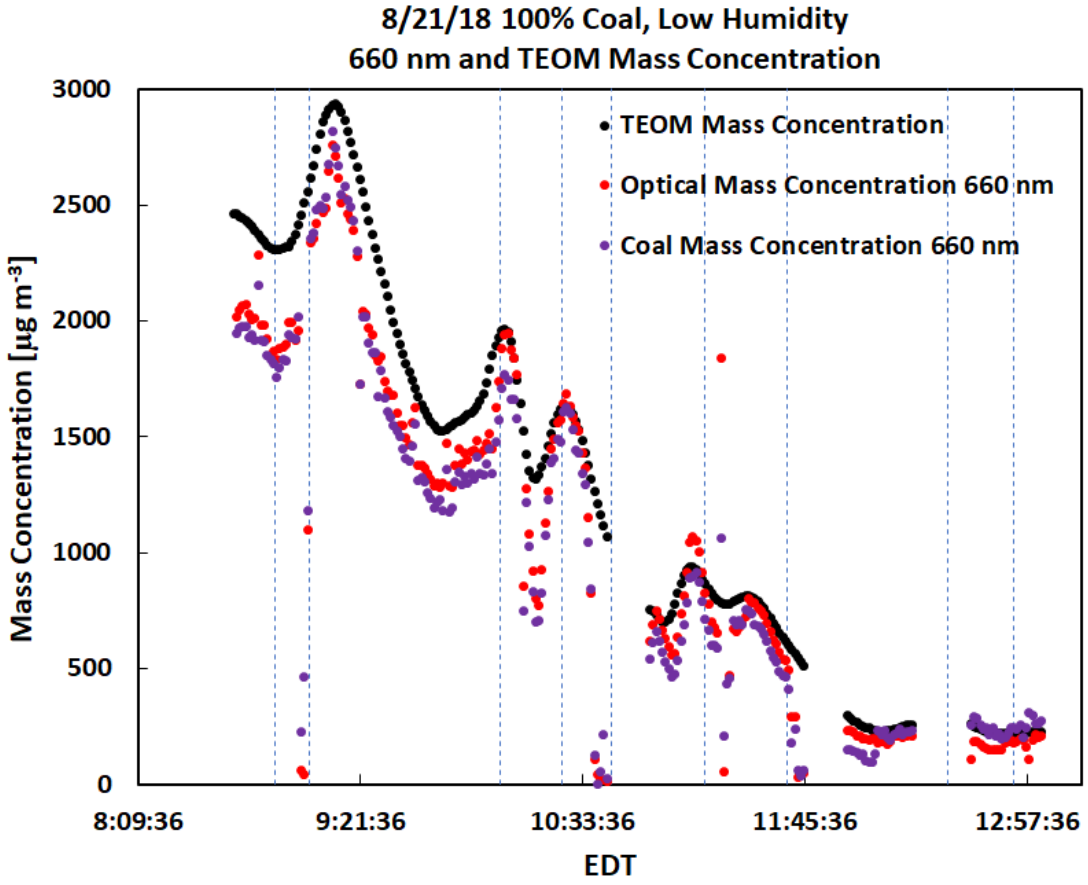

Figure 20. Time series of TEOM mass concentration and derived optical mass concentration from the prototype instrument. Coal (optical) mass concentration was achieved with the aerosol light absorption (scattering) measurement.

Figure 21 illustrates the data collected by the PDMs and TEOM during this test with 100% coal dust and low RH. The PDMs measure mass every minute and perform a mass concentration measurement every 30 min. To acquire the mass concentration values at every minute we divided the accumulated mass measurement in 1 minute by the flow measurement of 2.2 lpm for these samplers. For the most part, the PDMs follow the same trend as the TEOM with a larger quantity of noise. In particular, PDM3 has a noticeably larger amount of noise when compared with all other PDMs. This may be due to error within PDM3's mass measurements, or it could be due to the variation in locations of each PDM sampler within the testing chamber. The significant difference in noise between the PDMs and the TEOM suggest the method of mass concentration measurement performed by the laboratory TEOM is more accurate and precise than that of the PDM instruments. Comparing Figure 20 and Figure 21, it

can be seen that the optical measurements of aerosol mass have less noise compared with the laboratory TEOM that does the PDM instruments.

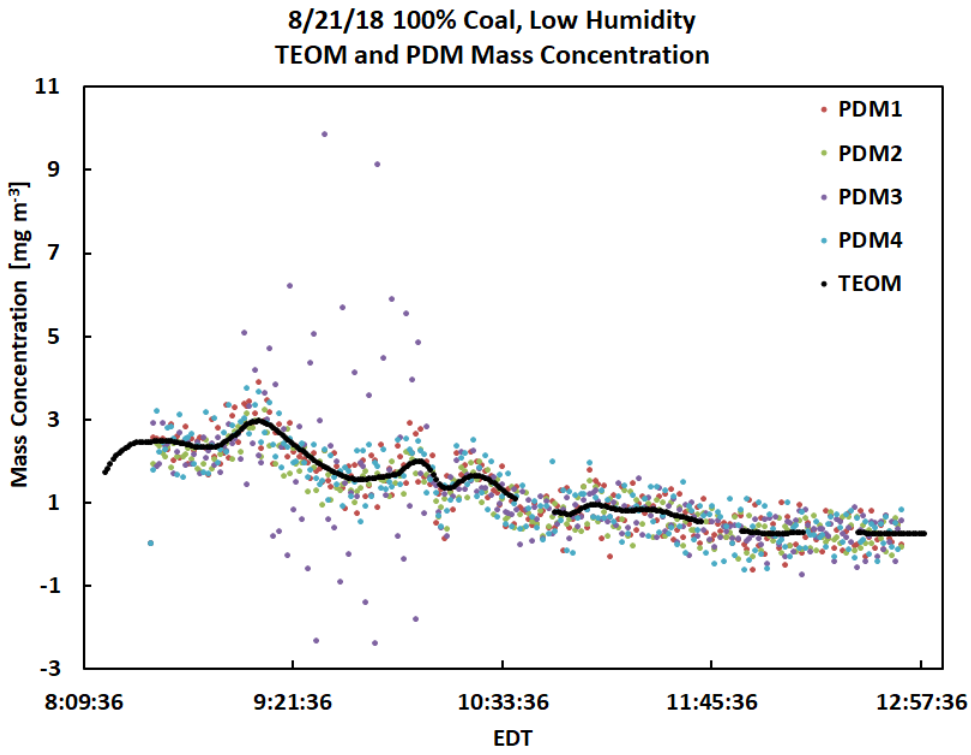

Figure 21. Comparison of four personal dust monitors and TEOM measurements for 1-minute time averages for each instrument for the low RH coal dust measurement.

100% Coal Dust 75% RH Test

The next test consisted of passing an aerosolized mixture of 100% coal dust through the two photoacoustic instruments, as well as the TEOM, PDMs and gravimetric samplers. Additionally, the relative humidity inside the testing chamber was adjusted to 75%. For the entirety of this test the 870 nm and 660 nm instruments were kept on the inlet system, with a flow rate of 2.2 lpm and a cyclone cutoff of 3.2 µm.

Figure 22 is a plot of TEOM mass concentration with respect to 660 nm absorption and scattering coefficients. Like testing on 8/21/18, the 100% coal dust concentration implies that we can assume all absorption and scattering were caused by coal dust, and we can calibrate our absorption and scattering mass concentration values to the TEOM values as shown schematically in Figure 15. Performing a linear fit to this data resulted in calibration factors for the 660 nm instrument of 1.56 (micrograms/cubic meter)/Mm^{-1} for scattering measurements and 1.35 (micrograms/cubic meter)/Mm^{-1} for absorption measurements. The high R^2values of 0.98 for both scattering and absorption data show a strong correlation with TEOM mass concentration measurements. Calibration factors were also determined for the 870 nm instrument following the same process (not shown) resulted in R^2 values of 0.98.

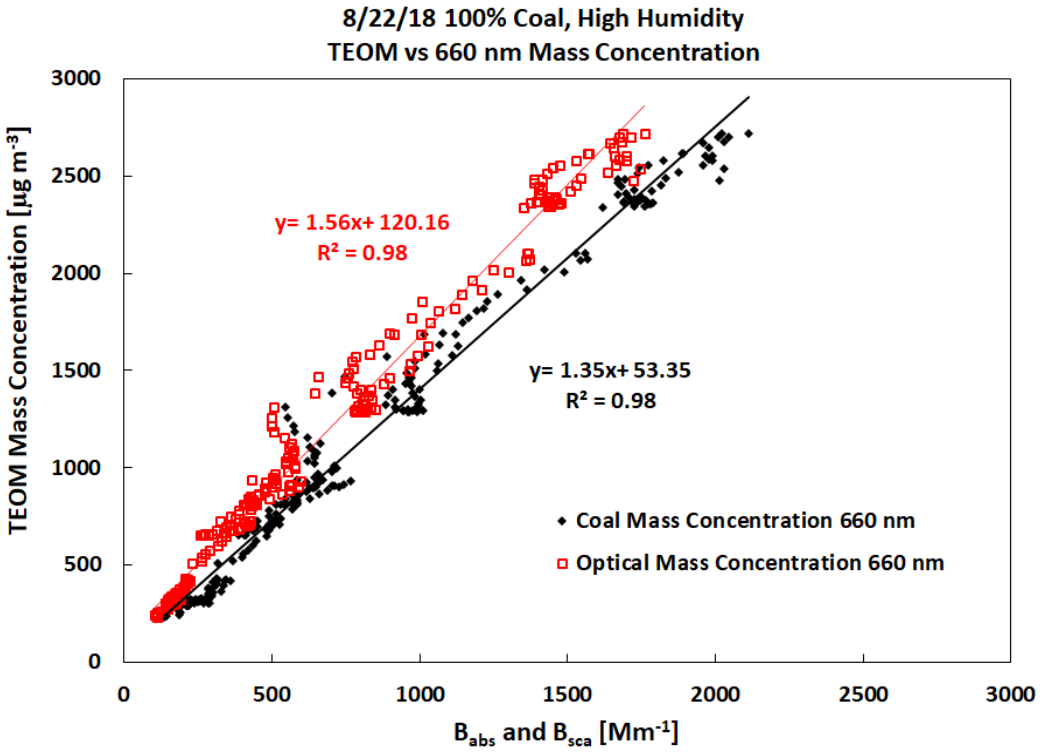

Figure 22. Scatter plot of TEOM mass concentration and aerosol scattering and absorption measurements for coal dust for 75% humidity.

The results of Fig. 22 are used to calibrate the instrument for coal dust and total dust measurements. The slope of the linear regressions are 1/*AE* and 1/*SE* for coal and total dust, respectively, referring to Eqs. (1) and (2). Thus the calibrated PM4 measurements are obtained from use of the equations

$$\boldsymbol{CoalDustPM4}\left[\frac{\mu g}{m^3}\right] = 1.35\left[\frac{g}{m^2}\right] * \beta_{abs}[Mm^{-1}] \quad , \tag{3}$$

$$\boldsymbol{TotalDustPM4}\left[\frac{\mu g}{m^3}\right] = 1.56\left[\frac{g}{m^2}\right] * \beta_{sca}[Mm^{-1}] \quad . \tag{4}$$

The specific units are given to ensure correct interpretation. We obtain the scattering and absorption efficient values in Eqs. (1) and (2) as *AE* = 0.74 m^2/gram and *SE* = 0.64 m^2/gram. Figures 7 and 8 show that the dominant aerosol diameter for these efficiencies is around 2 microns, and that these efficiencies do not depend strongly on coal type as they are in the geometrical optics regime.

The calibrated optical mass and coal dust concentrations from the prototype 660 instrument are shown as a time series along with the TEOM data in Figure 23. The data recorded by the 660 nm instrument has been time aligned, time averaged, and calibrated with the TEOM data. The data from the 660 nm instrument and the TEOM follow a strikingly similar

trend and the mass concentration values for the TEOM and 660 nm instrument are very close in value, which would be expected following calibration. It is also notable that the 660 nm data has a much smaller quantity of noise when compared with the data from 8/21/18 shown in Figure 20. This is likely due to the lack of adjustments made to the inlet system during 8/22/18 after the decision had been made to keep both photoacoustic instruments attached to the inlet system.

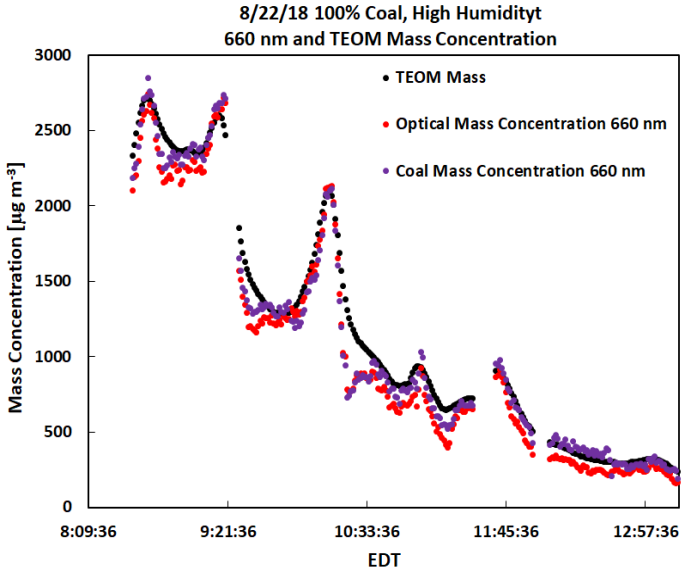

Figure 23. Time series of TEOM and optical total and coal dust mass concentrations from the prototype instrument for the 75% RH case.

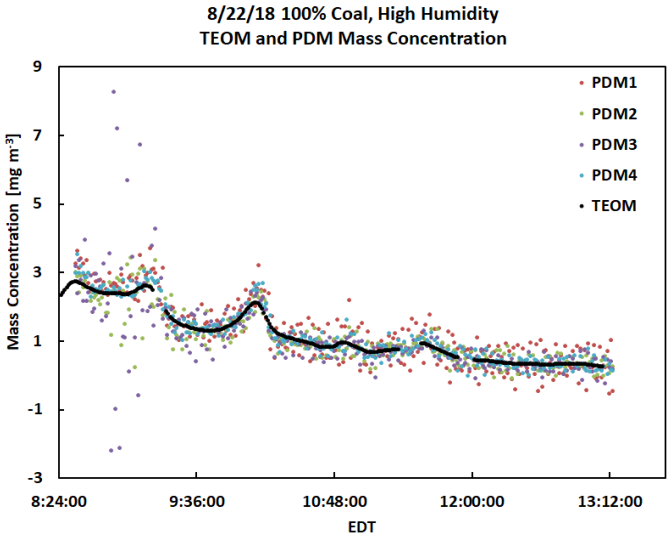

Figure 24. Comparison of four personal dust monitors and TEOM measurements for 1-minute time averages for each instrument for the 75% RH coal dust measurement.

Figure 24 displays a plot of the data collected by the TEOM and 4 PDM samplers. Looking at this data, it is clear that all four PDMs result in mass concentration values similar to that of the TEOM, further validating the TEOM data, though the data from each of the PDMs is noisy compared to that of the TEOM, indicating some uncertainties in mass measurements recorded by the PDMs.

75% Coal Dust 25% Silica Dust Low RH Test

The next test in the NIOSH facility consisted of passing an aerosolized mixture of coal dust and silica dust through the two photoacoustic instruments, as well as the TEOM, PDMs and gravimetric samplers to evaluate the optical instruments following the schematic in Figure 16. The proportions for this mixture were 75% coal dust and 25% silica dust by mass were loaded into the TSI Model 3400 fluidized bed aerosol generator. It is possible that the proportion of coal and silica dust delivered to the instruments had a different percentage after passage through cyclones and the rest of the system. The test was conducted with a relative humidity of approximately 25%. Three electron microscopy filters were used during this test with different exposure times determined by the scattering concentration at the time of filter insertion. The first filter was exposed for 2 minutes, the second filter for 4 minutes, and the final filter was exposed for 20 minutes.

Figure 25 is the scatterplot of the TEOM's mass concentration measurements with respect to the 660 nm instrument's measurements of coal dust mass concentration and total optical mass concentration obtained by multiplying the absorption and scattering measurements by the slopes of the curves in Figure 22, realizing the calibration evaluation procedure shown schematically in Figure 16. Coal dust is highly absorbing while silica dust is not, so the absorption detected during this test is primarily due to coal dust. Therefore, we can use the absorption measurements to determine the amount of coal dust present in the aerosol. The sample coal dust fraction was determined using the slope of linear fit for TEOM's mass concentration with respect to absorption. It was concluded that the sample coal dust fraction was 57% when coal dust was aerosolized with silica dust. We performed the same analysis to the data acquired from the 870 nm instrument and found the coal dust fraction to be 59% (not shown). These coal dust fractions calculated from the photoacoustic instruments vary significantly from the target concentration of 75% coal dust and 25% silica dust. The percentage of coal and silica dust by mass that is loaded into the fluidized bed aerosol generator does not necessarily reflect what becomes airborne, particularly in the size range of interest. In fact, NIOSH reported that their measurements of silica dust fraction using the FTIR method was 40% silica, 60% coal, in close agreement with our value of 57% coal dust.

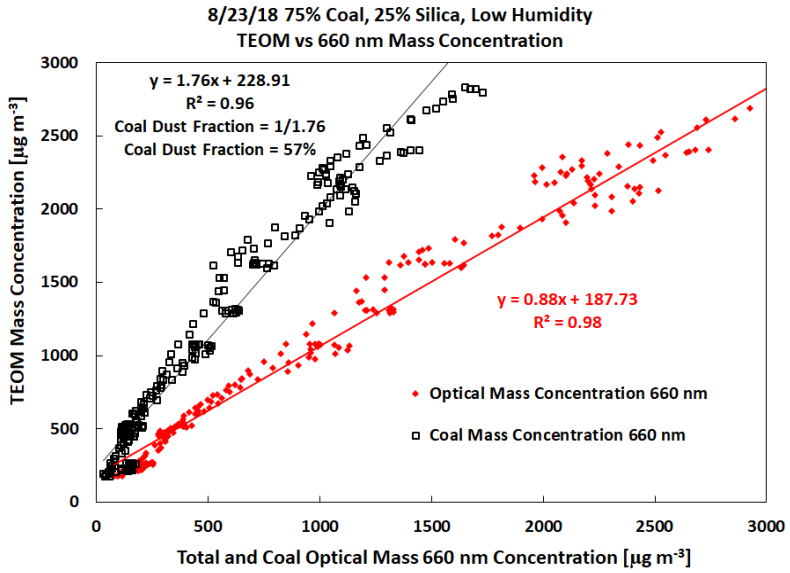

Figure 25. Scatter plot of TEOM mass concentration with optical total mass and coal dust mass concentration for the mixture of coal and silica dust. The coal dust fraction implied by the optical absorption measurement is 57%, compared with 60% obtained by NIOSH.

Figure 26 includes the time averaged optical and coal mass concentrations of the 660 nm instrument along with the TEOM mass concentration data. As seen in the data from the 100% coal dust test, the trends of the 660 nm data and the TEOM are strikingly similar. In addition, the mass concentration values from the scattering measurements match the TEOM data very closely. This is likely since the mass scattering efficiency of coal dust is about ½ that of silica dust, and the specific gravity of coal dust is about ½ that of silica dust. Since we are in the surface area regime for scattering measurements, these conditions make it so that the scattering measurements are equally sensitive to both coal and silica dust.

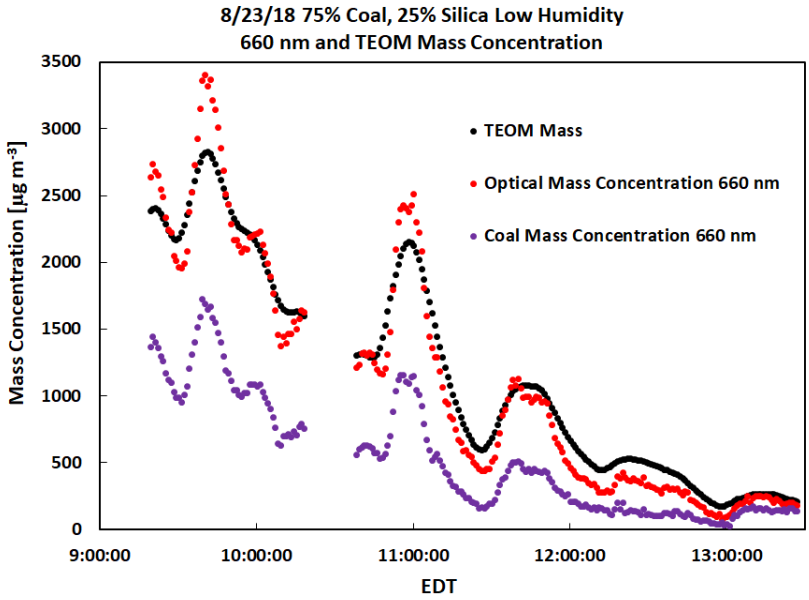

Figure 26. Time series of TEOM total aerosol mass concentration along with optical coal and total mass concentration for the coal-silica dust mixture.

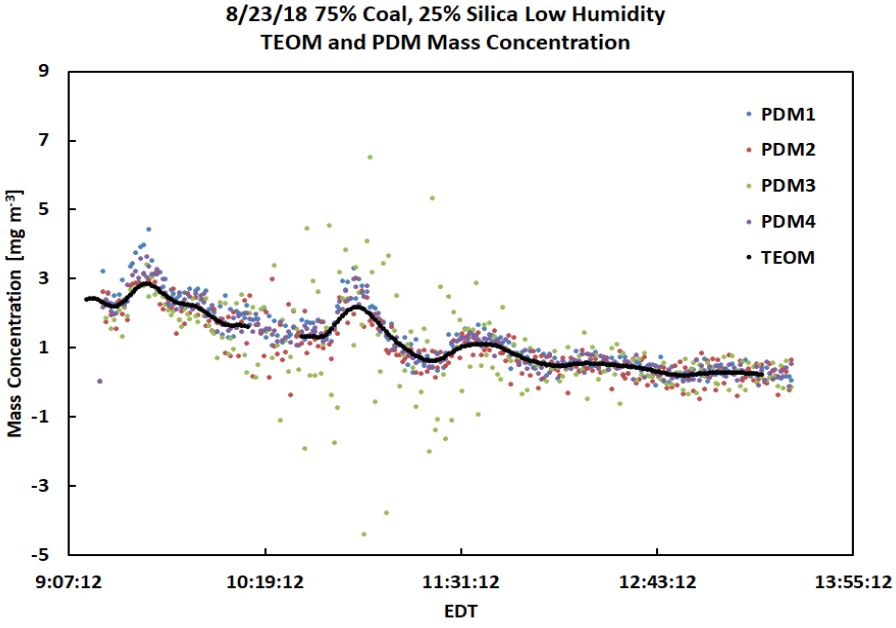

Figure 27. Comparison of four personal dust monitors and TEOM measurements for 1-minute time averages for each instrument for the 25% RH coal and silica dust measurement.

Figure 27 shows this test's mass concentration measurements collected by the TEOM and the four PDM samplers. The PDM values follow those of the TEOM moderately well, though

they are significantly noisier. As the PDMs only measure the mass deposited on a filter each minute, similar calculations were conducted to acquire mass concentration values as were done for the 100% coal dust test.

Extensive analysis of aerosol morphology and size were obtained by analyzing the nuclepore filters as discussed in Appendix 1. The nuclepore filters are a plastic membrane; therefore, measurements of carbon, hydrogen, and oxygen are against a large filter background. Other elements, especially those heavier than carbon, are readily identifiable. In summary, the following observations were made based on electron microscopy:

- Coal dust was predominantly carbon with negligible amounts of silica.
- 'Silica dust' was predominantly silica.
- Aerosol morphology was mostly compact angular grains, not spherical.

6.0 Technology Readiness Assessment:

Discussion of the project results

First we will start off with a discussion of the instrument performance under ideal laboratory circumstances where we measured either pure coal dust, or a combination of pure coal and silica dust. Optical measurements of coal dust aerosol mass concentration were empirically calibrated using the TEOM as a laboratory standard instrument as shown in Figure 15. Figure 23 and Figure 24 show the comparison of the TEOM total aerosol mass with the optical and PDM samplers, respectively, indicating less noise from the optical measurements. A similar comparison of total aerosol mass by TEOM, optical scattering, and the PDMs are shown Figure 26 and Figure 27. Aerosol light absorption measurements also allow for measurement of the coal dust concentration as shown in Figure 26. The reciprocal of the slope of the linear regressions for coal dust mass concentration and aerosol light absorption and scattering measurements in Figure 22 revealed that the dominant aerosol diameter was 2 microns. Thus the relevant regime is geometrical optics as noted by where 2 microns intersects the theoretical scattering and absorption efficiency curves in Figure 6, Figure 7, and Figure 8, ***ideal for greatly reducing sensitivity to coal and total dust composition and aerosol size, made possible by the practical choice of using inexpensive 660 nm lasers.*** Optical scattering measurements have often been used in instruments as a proxy for aerosol mass concentration because of the high precision. It should be noted that the experiment described here was with ideal mixtures of relatively pure coal and silica dust having a size distribution determined by the aerosol generator and the instrument cyclones. Optical measurements of total dust (light scattering) and coal dust (light absorption) are promising for real time measurements of these dust quantities. Additional measurements for other dust mixtures, and including aerosol size distribution measurements by the aerosol particle sizer are needed to evaluate the robustness of these results. Use of a microcontroller based lock-in amplifier for the prototype portable instrument makes lower cost, lower power need, and smaller instrument size a realistic proposition. Additional engineering is readily doable to further reduce the size of the instrument.

Discussion of Additional Measurement and Instrument Needs

Our instrument goal is to develop a portable prototype instrument for coal and silica dust mass concentration. Our laboratory demonstration at the NIOSH facility considered an ideal combination of pure coal and pure silica dust with no complications due to submicron combustion aerosol or other mine minerals like kaolinite. Our use of scattering measurements for total dust mass concentration and absorption measurements for coal dust concentration can provide coal dust concentration when submicron aerosol such as diesel particulate matter elemental carbon is not present, and only an upper limit for silica dust concentration when other minerals such as kaolinite are present, or submicron combustion aerosol. The total scattering is due to all suspended particulate matter. The absorption measurement is specific to coal dust when no elemental carbon from diesel particulate matter is present. An expanded laboratory campaign could include the following:

- Measurements at the NIOSH Marple chamber mixing diesel particulate matter, coal dust, and silica dust.
- Use of one of our prototype instruments for measuring PM4 total respirable dust with use of a 4 micron cyclone.
- Use of a second of our prototype instruments with a PM1 impactor to measure only the submicron aerosol mass concentration from diesel particulate matter.
- Use of a NIOSH SMPS instrument to measure submicron aerosol size distribution.
- Use of a NIOSH APS instrument to measure total aerosol size distribution to 10 microns.
- Use of a NIOSH TEOM equipped with a PM4 cyclone to measure total aerosol mass concentration.
  Use of a NIOSH TEOM equipped with PM1 impactor to measure submicron aerosol mass concentration.
- Use of NIOSH EC/OC measurements for both PM1 and PM4 size cuts.
  Evaluate the ability of two of our prototype instruments for separating and obtaining PM1 total and elemental carbon mass concentration, and PM4 for total dust and coal dust concentration in the presence of submicron aerosol

Additional refinements to our current approach should include the following:

- Reduce the size of the current instruments by placing them in a more compact enclosure.
- Replace the total scattering measurement with a single particle aerosol light scattering measurement made using the same laser beam so that the instrument can provide for aerosol size distribution measured optically, for better discriminating between PM1 and PM4 in our instrument.
- Develop a very compact micro electro mechanical resonator for PM1 diesel elemental carbon mass measurements based on modified quartz enhanced tuning fork spectroscopic measurements made appropriate for aerosol sampling in addition to trace gas detection (Kosterev et al. 2005).
- NIOSH is further developing the filter based method for separating quartz dust and kaolinite dust by spectroscopic measurements of aerosol collected on a filter by use of a Fourier Transform Infrared Spectrometer (Miller et al. 2017). Our photoacoustic aerosol light absorption measurements of coal dust are species specific because coal dust absorbs strongly at

the instrument wavelength 660 nm. Our photoacoustic sensor uses a microphone to measure the sound created when light is absorbed, so any laser wavelength can be used as long as appropriate optical windows are used in the instrument (easy to do). We propose to develop a real time spectroscopic silica dust monitor to add to the coal dust monitor that will be selectively able to quantity silica dust concentration in a working mine environment where other minerals are suspended as aerosol. The proposed instrument will use aerosol light absorption measurements at 12.5 microns wavelength to obtain the combination of silica and kaolinite dust concentration, and measurements at 10.9 microns to quantify kaolinite dust concentration. Kaolinite dust is the primary interference for the 12.5 micron measurement of silica dust. Any coal dust interference could be mitigated by having spectroscopic measurements at 660 nm. Our demonstration of use of an inexpensive microcontroller for data acquisition in the current project makes it reasonably priced to consider use of 3 acoustical resonators as shown in Figure 10 without incurring excessive cost. We may use quantum cascade lasers (Consolino et al. 2019) for this application.

7.0 Appendices:

Appendix 1. Electron Microscopy Analysis of Coal and Silica Dust Aerosol

Aerosol were collected on nuclepore filters for analysis with the electron microscope at the University of Nevada Reno. After utilizing a scanning electron microscope (SEM) to produce images and to perform Energy Dispersive Spectroscopy (EDS) with two electron microscopy filters, one from the 100% coal test day and one from the 75% coal 25% silica test day, the following data was compiled pertaining to the size distribution, morphology, and elemental composition of the collected particles.

SEM Results 100% Coal

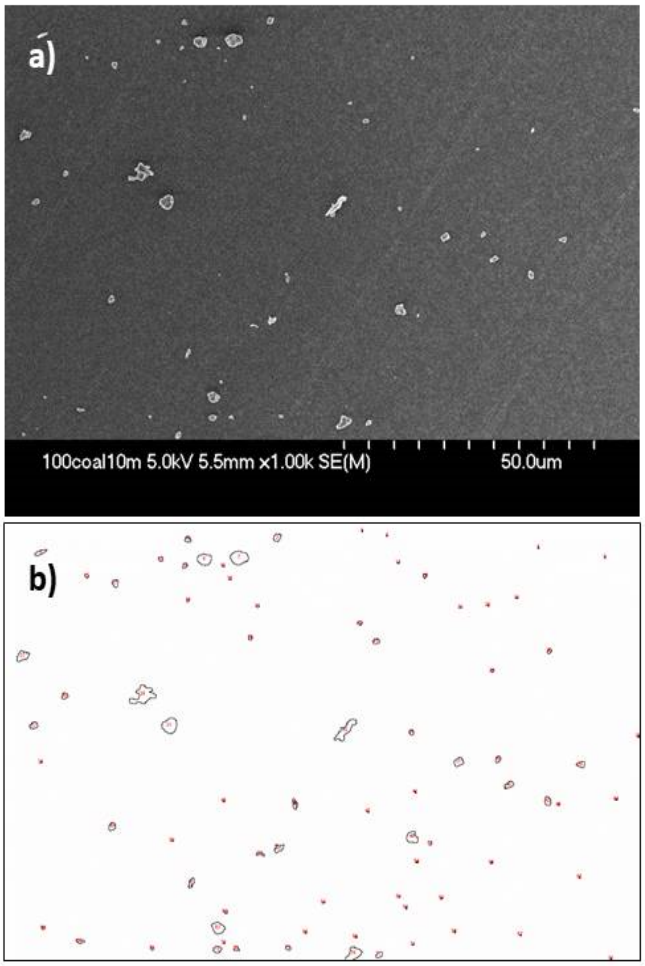

Figure 28. a) SEM image of the aerosol captured on a filter that was exposed to a sample of 100% coal at the NIOSH lab in Pittsburgh. The filter was exposed to aerosol for 10 minutes. B) Image generated with ImageJ's particle analyzer tool. This image displays the outlines used to calculate particle areas.

Utilizing the SEM images and the software ImageJ, the particles in the images were analyzed to determine their size distribution. A variety of images were collected of different scales, so it was necessary to set the scale in ImageJ during each image analysis. Many images were taken with a similar scale as displayed in Figure 28a to include a large quantity of particles. To determine the particle size distribution from these images, the particle analyzer tool in ImageJ was used after thresholding an image to generate a series of outlined particles as shown in Figure 28b. The area within the particle outline is calculated in ImageJ and used to calculate the size distribution of particle diameters. In images taken at a smaller scale which only include a single particle such as Figure 31, the measure tool in ImageJ was used to measure the length and width of the particle rather than using the particle analyzer to determine the area. After compiling all of the diameter, length, and width measurements from ImageJ into one table, the histogram shown in Figure 29 was created. It is interesting to note that the majority of particles analyzed for this filter exist in the range between 0.5-1 µm. This may be an explanation for the lack of scattering and absorption fluctuations during inlet system changes on 8/21/18. Since the majority of particles were far under the cyclone's particle cutoff of either 3.2 µm or 4 µm, altering the flow rate into the cyclone wouldn't have a noticeable effect on the particle size distribution that makes it into the resonator.

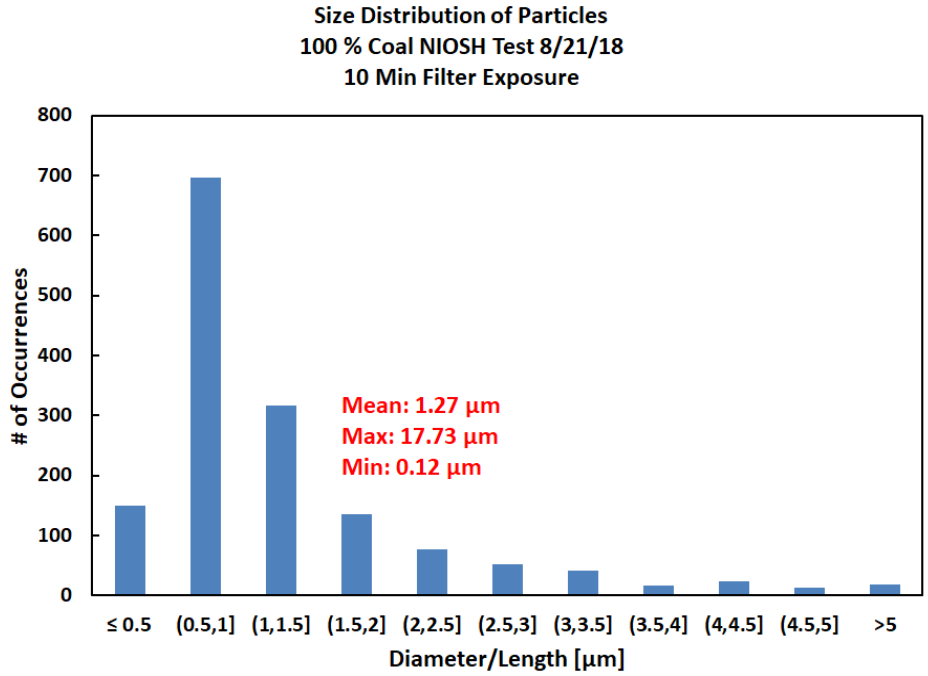

Figure 29. Particle size distribution on a filter exposed to a sample aerosol of 100% coal for 10 minutes.

More images were taken at smaller scales to determine the general morphology of the sample aerosol. In the case with 100% coal, the particles varied in shape as shown in Figure 30 and Figure 31. Some particles appear to be spherical in shape, however there are many that

exist in more irregular forms. Some of this variation in morphology may be due to the process used to create the aerosolized dust with the fluidized bed aerosol generator.

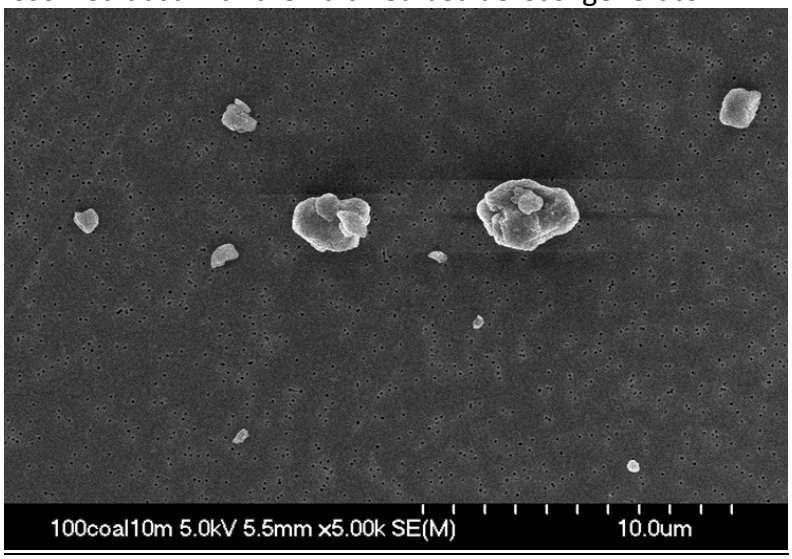

Figure 30. SEM image of particles captured on a filter that was exposed to a sample of 100% Coal for 10 minutes at the NIOSH lab in Pittsburgh.

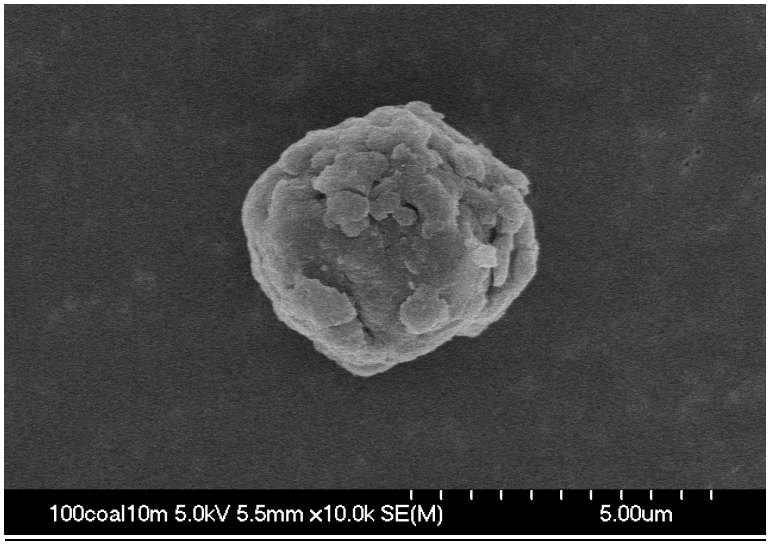

Figure 31. Same as previous figure.

Throug

h EDS we were able to obtain information on the elemental composition of some of the particles captured on the polycarbonate nuclepore filter. Before placing the filter in the SEM for analysis, a platinum film was applied using a platinum sputter coater. Due to the prevalence of carbon, oxygen, and platinum on the nuclepore filter and film coating, the elemental composition analysis was not able to detect the presence of these elements in individual particles apart from the filter and film background. This can be seen in Figure 32, where only a region of the particle was selected for analysis, but the presence of carbon and oxygen is overwhelming compared to the presence of aluminum and silicon. Despite this limitation, EDS led to an insightful analysis of impurities that may have existed in the sample aerosol of 100%

coal. For example, using EDS to perform an analysis on 18 different images including about 76 particles resulted in the detection of aluminum and silicon impurities in only 4 particles. Additionally, the atomic percentage of aluminum and silicon was below 1.2% for all 4 particles with carbon and oxygen making up the majority. Although this measurement of atomic percentage is skewed with the overwhelming presence of carbon, oxygen, and occasionally platinum, it is still useful in concluding that the majority of particles analyzed did not have impurities. This lack of impurities leads to the conclusion that the coal sample was primarily composed of carbon.

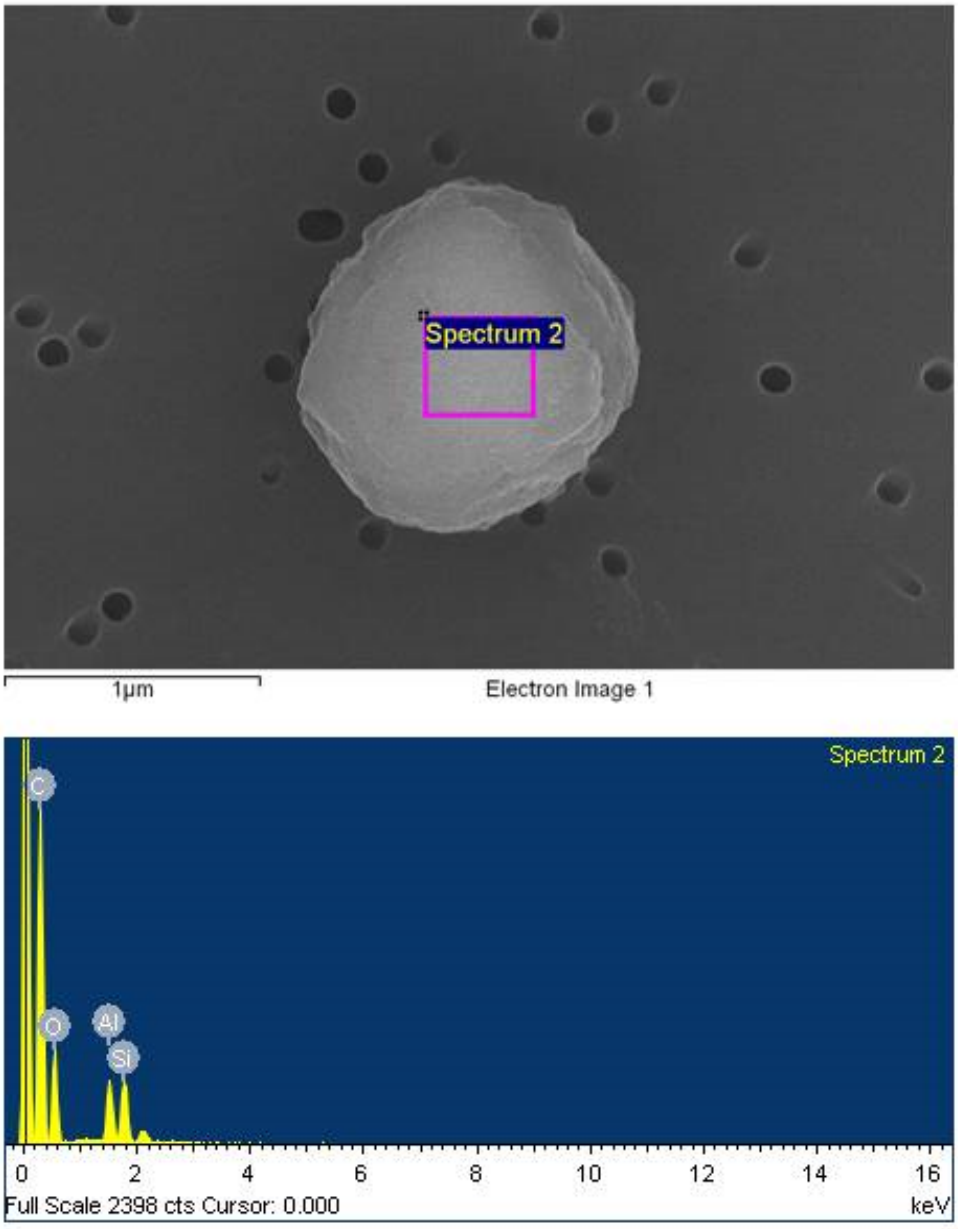

Figure 32. SEM image and EDS elemental composition plot of a particle found on a filter exposed to a sample aerosol of 100% coal for 10 minutes.

SEM Results 75% Coal 25% Silica

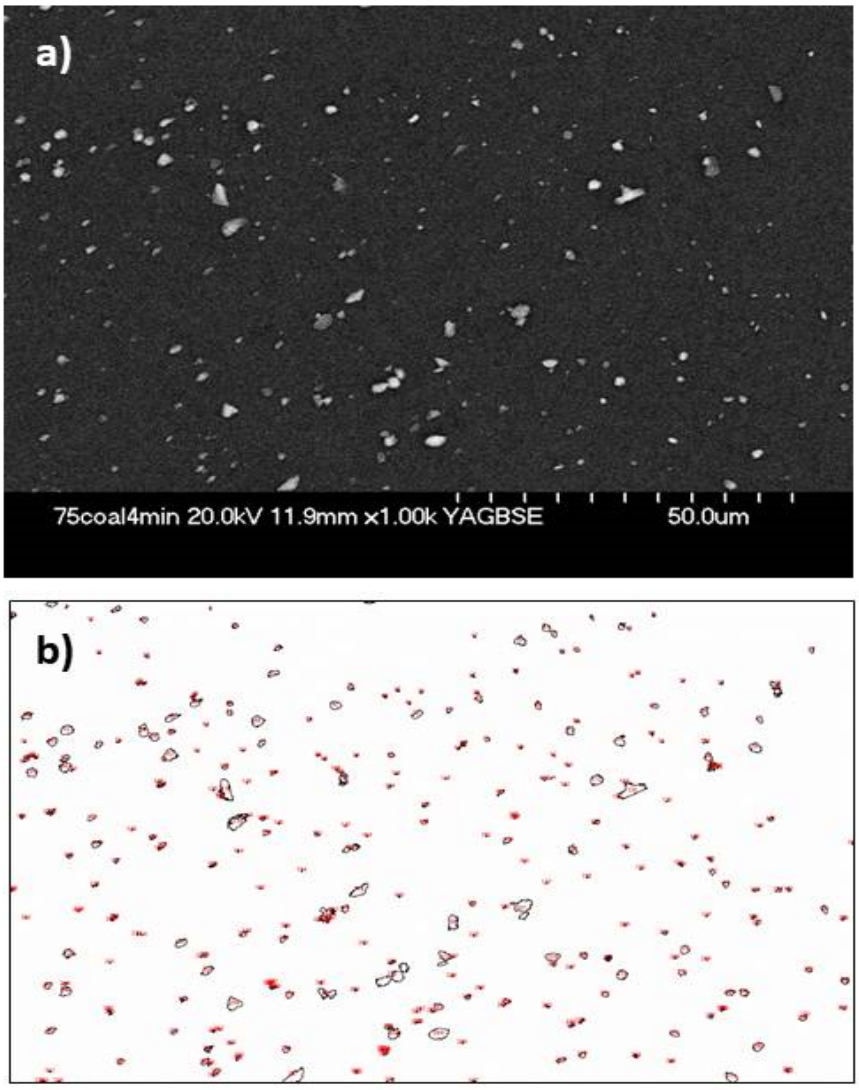

Figure 33. a) SEM image of the aerosol captured on a filter exposed to a sample of 75% Coal and 25% Silica at the NIOSH lab in Pittsburgh. b) Image of particle outlines generated with ImageJ's particle analyzer tool.

The SEM images acquired from the filter exposed to 75% coal were analyzed in the same way as previously mentioned, using ImageJ's particle analyzer and measure tools. This process is depicted in Figure 33. After all images were analyzed and the information about length or diameter of each particle was compiled into excel, the histogram shown in Figure 34 was generated. It is interesting to note that the majority of particles on this filter existed in the sub-micron range below 0.5 μm, whereas the majority of particles on the filter exposed to 100% coal existed in the range between 0.5-1 μm. The majority of particles may have been smaller during the test with 75% coal and 25% silica due to differences in the effects of grinding and aerosolization on coal versus silica. It is possible that the silica was more readily

deagglomerated and broken up into smaller particles than coal inside the fluidized bed aerosol generator. There may have also been differences in the processes for grinding up the coal and silica into a powder before the samples entered the fluidized bed aerosol generator. The average particle sizes in the case with 75% coal and 100% coal were 0.75 µm and 1.27 µm respectively, which agree with the estimates made based on absorption and scattering measurements.

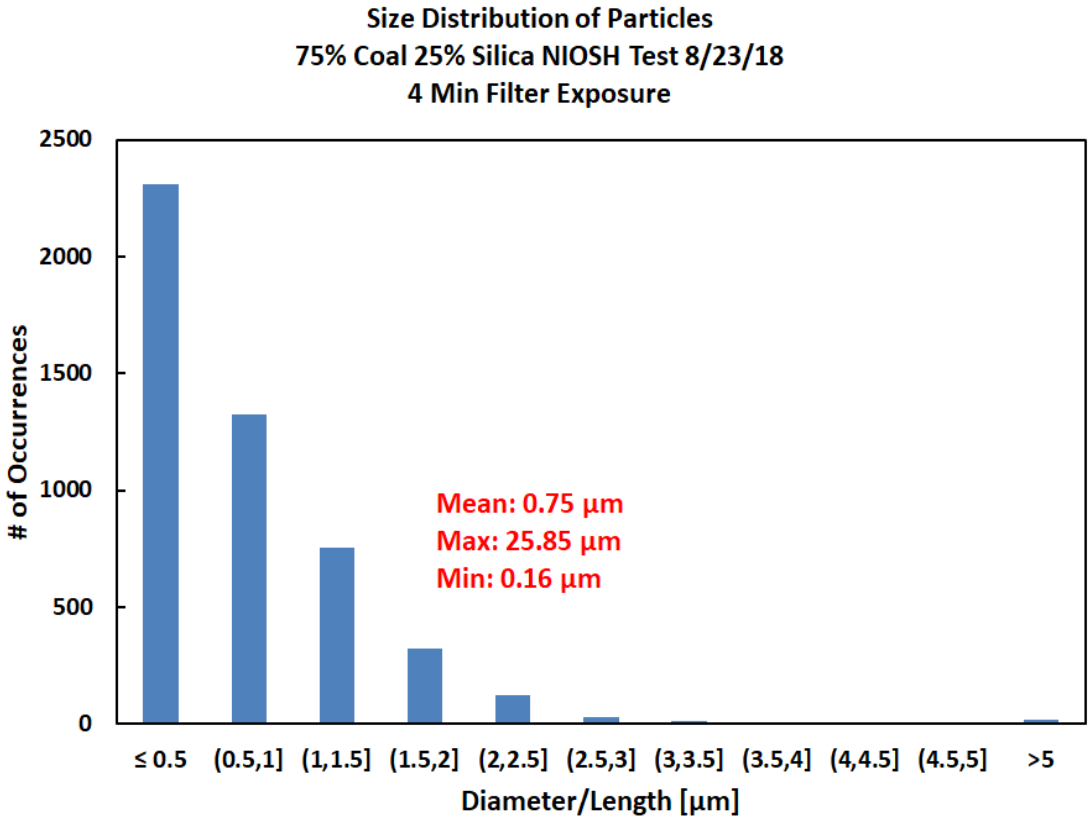

Figure 34. Particle size distribution on a filter exposed to a sample aerosol of 75% coal and 25% silica by mass for 4 minutes.

In Figure 35 you can see a broad image of multiple particles and their differing morphology. The particles in this image range in size between 0.2-4 µm and exist in many irregular forms, which is consistent with the particles from the test with 100% coal dust. Another interesting thing to note about Figure 35 is the obvious difference in brightness between the different particles. It was found that the brighter particles tended to be silica and the darker particles were coal. This certainly agrees with the higher scattering properties of silica in comparison with coal.

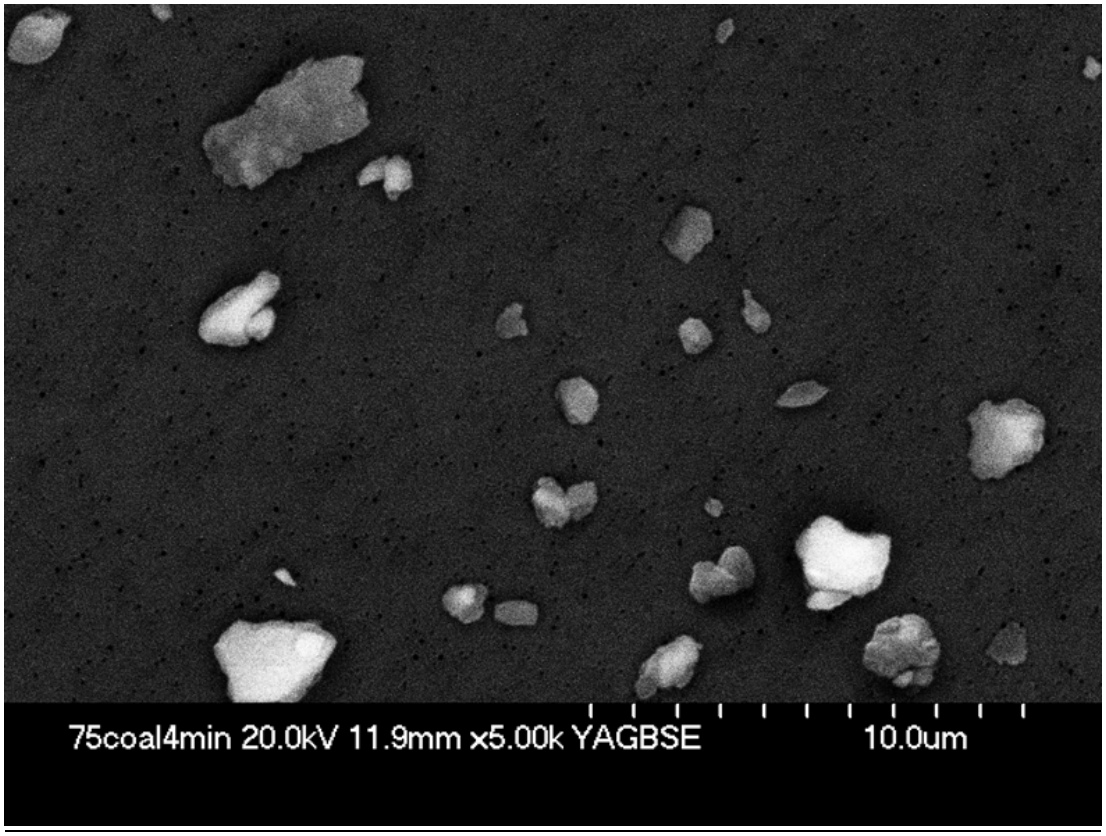

Figure 35. SEM image of particles collected on a filter exposed to an aerosolized sample of 75% coal and 25% silica by mass. The filter was exposed to aerosol for 4 minutes.

In Figure 36 images of 3 particles at different degrees of tilt is displayed. Viewing these particles at different angles gives us more insight about particle size in all dimensions, as well as morphology in all dimensions. Viewing these particles at a 60-degree tilt reveals the height of the particles to exist between about 1-3 μm. Additionally, the particles appear to have irregular shapes when viewed at a tilt.

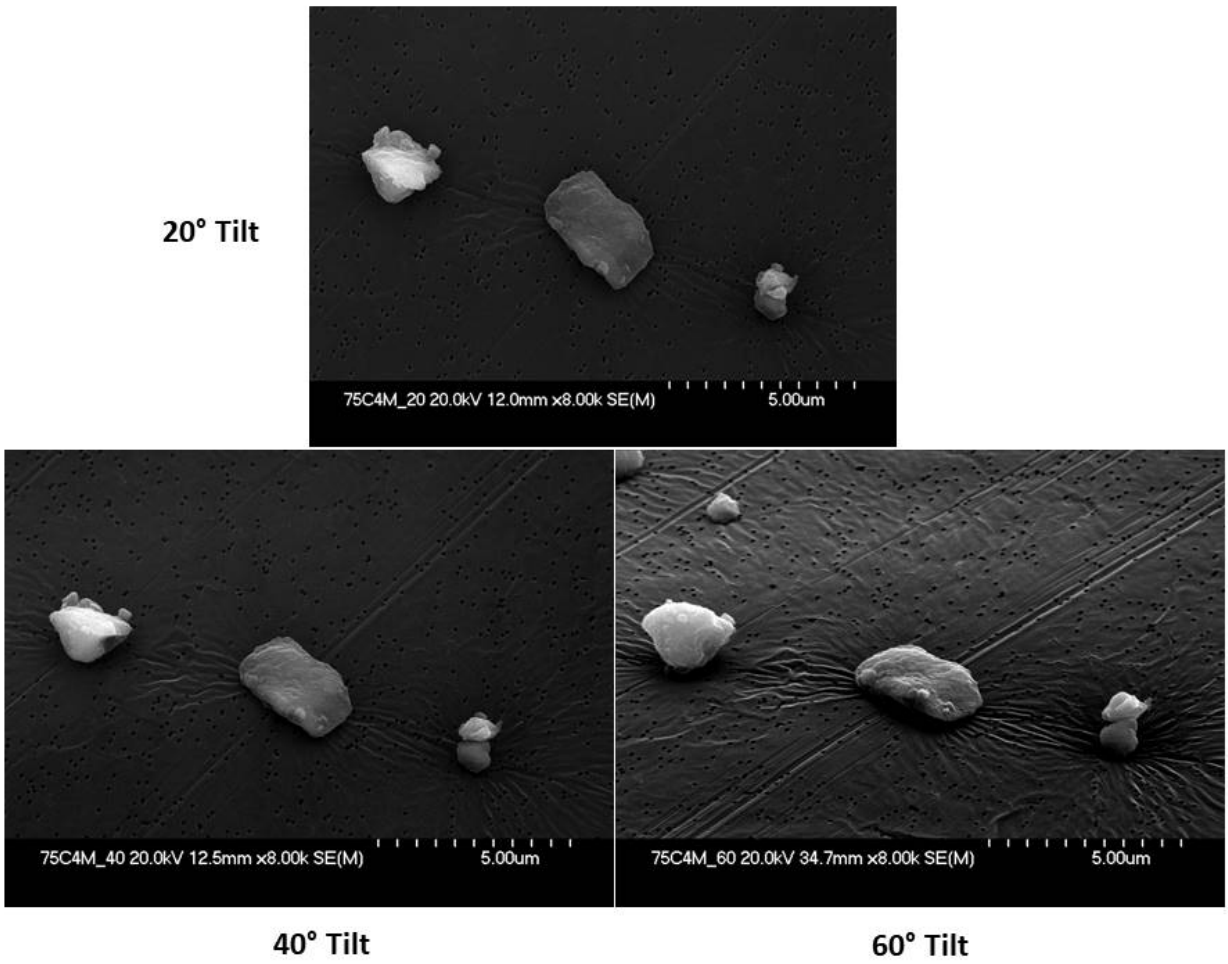

Figure 36. SEM images of 3 particles collected on a filter exposed to an aerosol of 75% coal and 25% silica by mass. Images of particles were taken at 20, 40, and 60 degree tilts.

In Figure 37 the same 3 particles which were shown in Figure 36 are displayed along with the elemental composition of each particle. The elemental composition was determined using EDS and is depicted by the colored plots. This analysis was performed by drawing a line through all 3 particles and the background. The elemental composition is determined at each point along the line and plotted on the y-axis of each plot. Looking at the plots for silicon, oxygen, carbon, and platinum, it is clear that these 3 particles are silica rather than coal due to the abundance of silica and oxygen in each particle. It is also interesting to note the high amount of carbon present due to the polycarbonate filter. The high carbon background causes small amounts of carbon present in each of the 3 particles to be undetectable, as shown in the figure below.

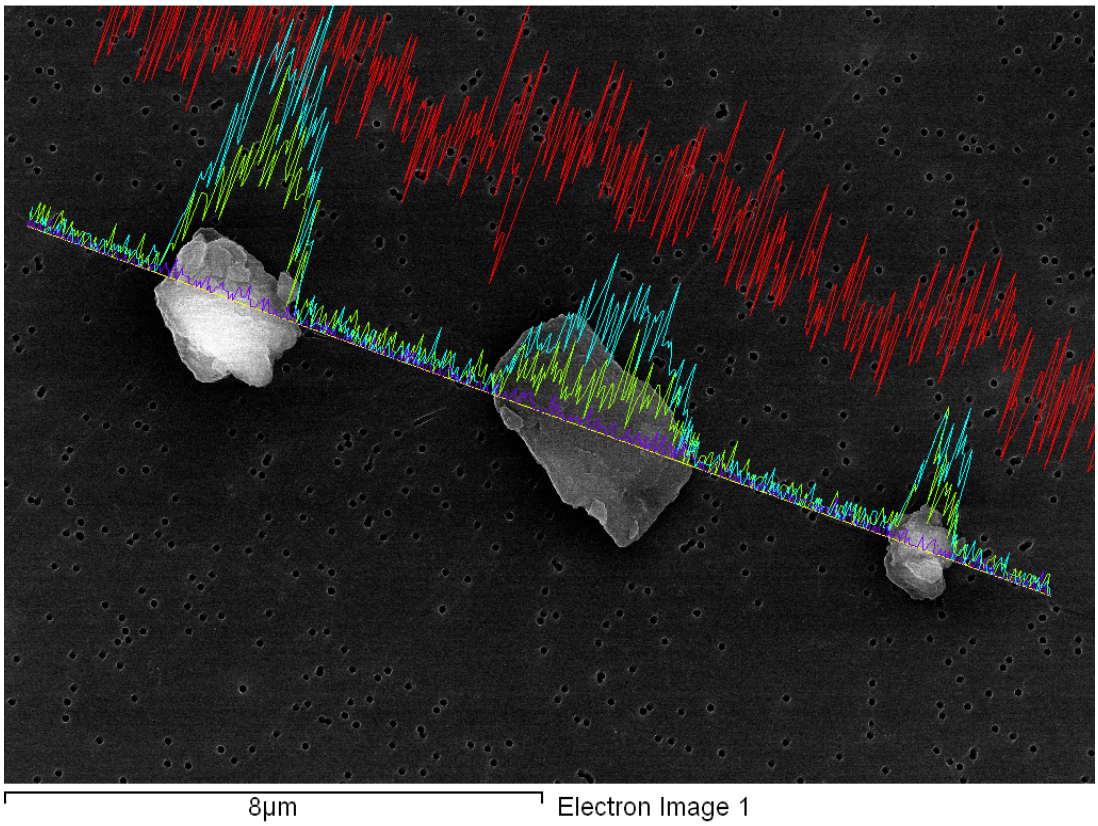

Figure 37. Image generated during EDS analysis of 3 particles collected on a filter exposed to a sample of 75% coal and 25% silica by mass. The plots depict the amount of each element measured at the yellow line during a line analysis. Red is carbon, blue is silicon, green is oxygen, and purple is platinum.

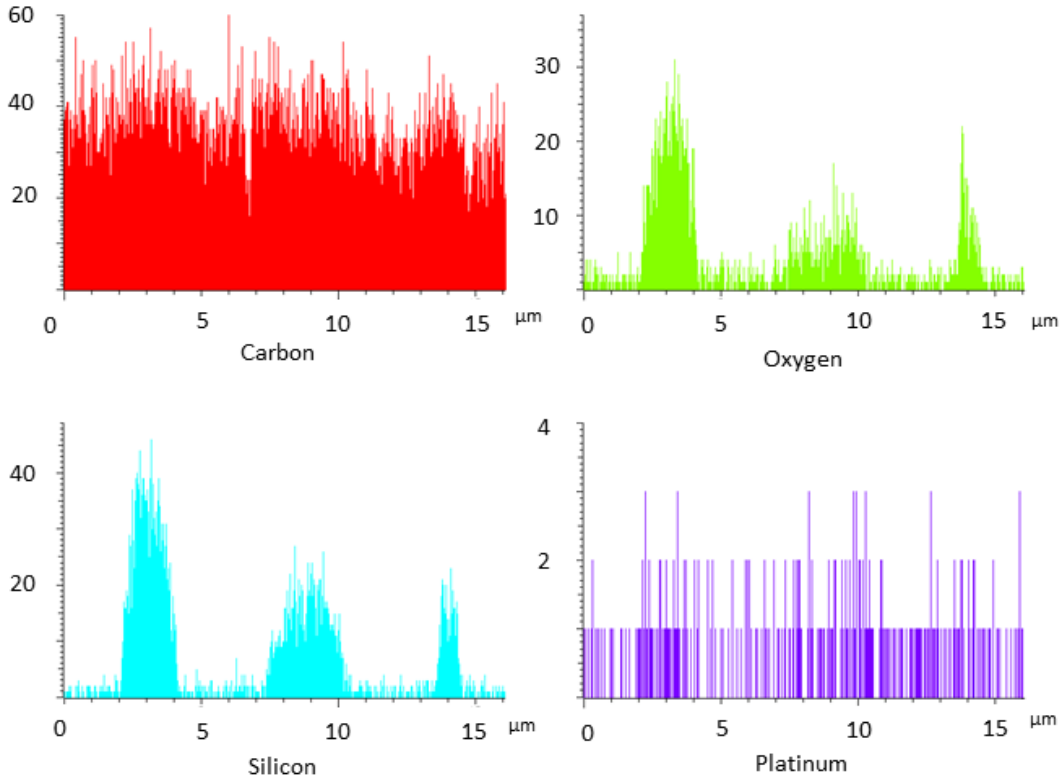

Figure 38. Individual plots of carbon, oxygen, silicon, and platinum presence in the 3 particles above.

Appendix 2. Microcontroller-Based Photoacoustic Instrument Description

This Appendix describes the use of the Teensy 3.6 microcontroller and PJRC audio adapter boards (Figure 39. Two PJRC Audio Adaptor Boards configured to operate with a Teensy 3.6.Figure 39) to operate the battery powered prototype instrument.

Audio Card Operation and Lock-in Amplification

The instrument uses two PJRC Audio Adaptor Boards in conjunction with a Teensy 3.6 microcontroller to detect by lock-in amplification the microphone, scattering photodiode, and extinction photodiode (laser power) signals. These inputs are represented by the *i2squad1* object in Figure 40. The Audio Adaptor Boards also produce signals (*sineX*, *sineY*, and *sineSpkr*) to drive the speaker, to modulate the laser, and to perform lock-in amplification.

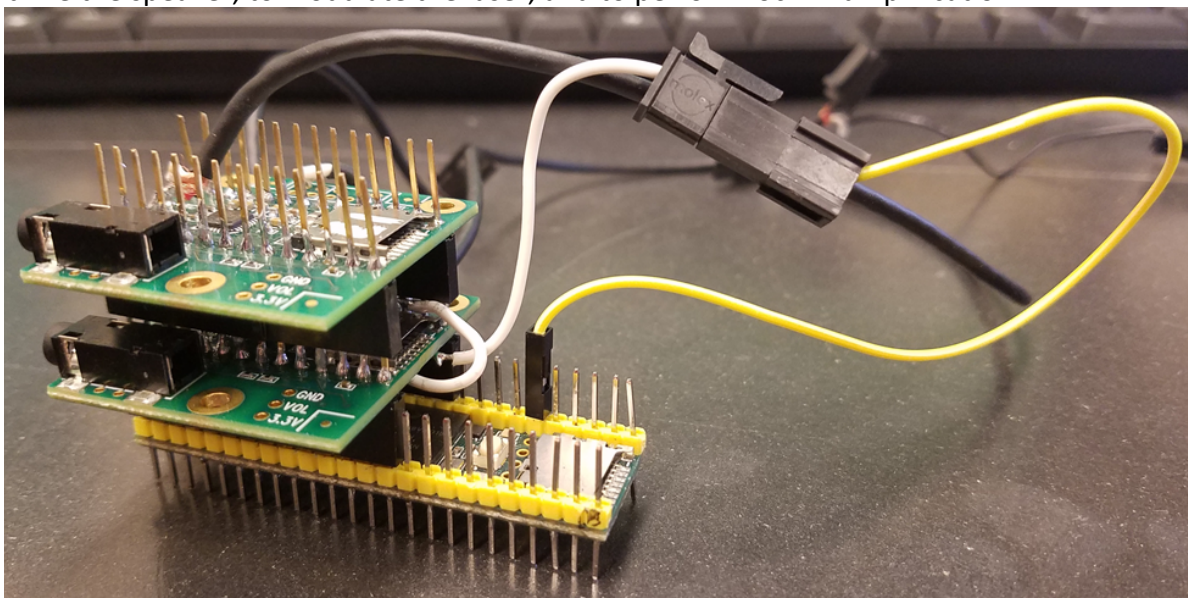

Figure 39. Two PJRC Audio Adaptor Boards configured to operate with a Teensy 3.6.

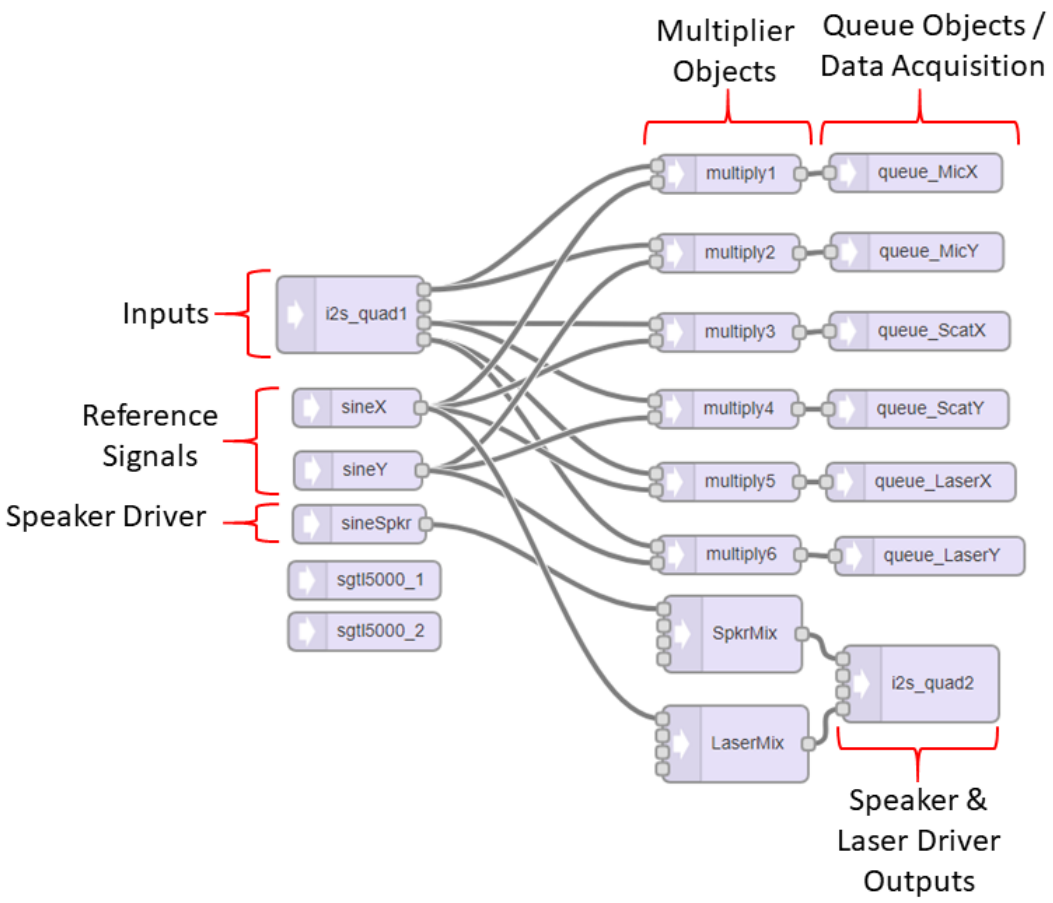

Figure 40. This audio design was generated by PJRC's online Audio System Design tool, which in turn generates code for the Teensy. This code allows the Audio Adaptor Boards to send and receive audio signals, perform calculations on the signals, and output data serially.

Lock-in amplification allows us to detect a response signal even in the presence of comparatively high background noise by singling out a narrow frequency band of signal and eliminating noise at all other frequencies. During phase-sensitive detection, an internal reference signal in the amplifier is phase-locked to an external reference, in our case, the laser excitation signal. The internal reference is described by Eq. (1) and is represented by the *sineX* object in Figure 40

$$V_{ref} = V_L \, sin\left(\omega_L t + \theta_{ref}\right) . \quad (1)$$

The measured signal, Eq. (2), is received from the input object *i2squad1*

$$V_{meas} = V_{sig}\sin\left(\omega_L t + \theta_{sig}\right). \quad (2)$$

The measured signal Eq. (2) is multiplied by the reference Eq. (1), generating a DC offset and an oscillating signal. This multiplication is represented by *multiply1*, *multiply3*, and *multiply5* in Figure 40 and by Eq. (3):

$$V_{sig}V_L\sin\left(\omega_L t + \theta_{sig}\right)\sin\left(\omega_L t + \theta_{ref}\right) = \frac{V_{sig}V_L}{2}\cos(\theta_{sig} - \theta_{ref}) - \frac{V_{sig}V_L}{2}\cos(2\omega_L t + \theta_{sig} + \theta_{ref}) . \quad (3)$$

The second term on the right-hand side is double the frequency of the reference oscillator, and is eliminated by a low-pass filter, allow us to obtain the desired frequency component V_{sig}. The result is the in-phase component X of the signal amplitude relative to the lock-in reference. A second phase-sensitive detection is performed with a reference that is π/2 radians out of phase with the external reference. This process allows us to determine the phase dependence from the initial in-phase component and yields the quadrature component Y. This time, the *sineY* object and the input signals are multiplied in *multiply2*, *multiply4*, and *multiply6* to calculate the quadrature component.

$$V_{sig}V_L\sin\left(\omega_L t + \theta_{sig}\right)\sin\left(\omega_L t + \theta_{ref} + \frac{\pi}{2}\right) = \frac{V_{sig}V_L}{2}cos(\theta_{sig} - \theta_{ref} - \frac{\pi}{2}) - \frac{V_{sig}V_L}{2}\cos(2\omega_L t + \theta_{sig} + \theta_{ref} + \frac{\pi}{2}) . \quad (4)$$

These two phase-sensitive detection procedures yield the in-phase component X, the quadrature component Y, the overall magnitude of the measured signal R, and the phase between the signal and the lock-in reference φ. These four products of the lock-in amplification process are defined in Eqs. (5) – (8),

$$X = \frac{V_{sig}V_L}{2}cos\ (\theta_{sig} - \theta_{ref}) \quad (5)$$

$$Y = \frac{V_{sig}V_L}{2}sin\ (\theta_{sig} - \theta_{ref}) \quad (6)$$

$$R = \sqrt{X^2 + Y^2} = \frac{V_{sig}V_L}{2} \quad (7)$$

$$\varphi = tan^{-1}(\frac{Y}{X}) = \theta_{sig} - \theta_{ref} . \quad (8)$$

The X and Y components of each signal are passed to the queue objects, where they can be accessed by the rest of the Teensy code and used to determine the overall magnitude R of each signal. Lockin amplification is used for obtaining microphone (light absorption), photodiode (light scattering), and laser power signals at the operating frequency.

Teensy 3.6 Microcontroller Instrument Operations

The instrument conducts data acquisition and processing via a Teensy 3.6 microcontroller programmed within the Arduino IDE. The Teensy code executes the algorithm illustrated in Figure 41 and described below.

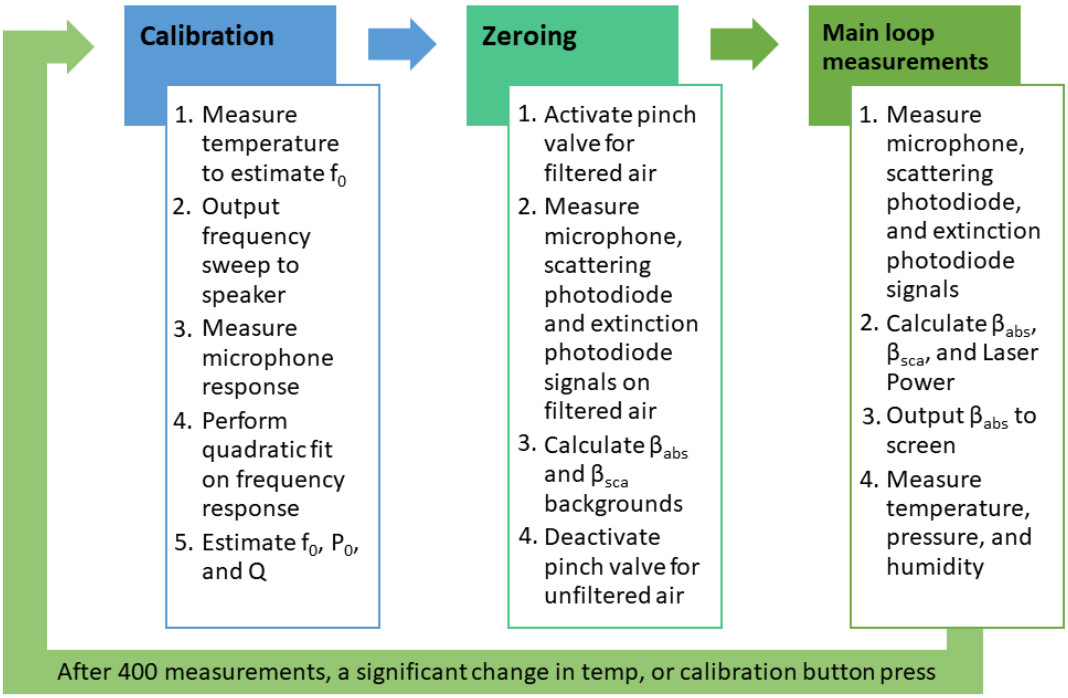

Figure 41. Flow chart demonstrating the algorithm of the photoacoustic instrument.

The instrument conducts acoustic calibration immediately upon power-up. First, it measures the temperature inside the resonator in order to estimate its resonance frequency f_0. Next, the speaker is driven at a frequency range surrounding the initial f_0 estimate and the microphone signal is recorded. Microphone pressure as a function of frequency can be expressed as:

$$|P(f)|^2 = \frac{{P_0}^2}{1+(\frac{2Q(f-f_0)}{f_0})^2} \quad , (9)$$

where P_o is the peak pressure at resonance, and Q is the quality factor. The reciprocal of the microphone signal recorded during this frequency sweep yields the reciprocal of a resonance curve resembling a quadratic function, like the one in Figure 42.

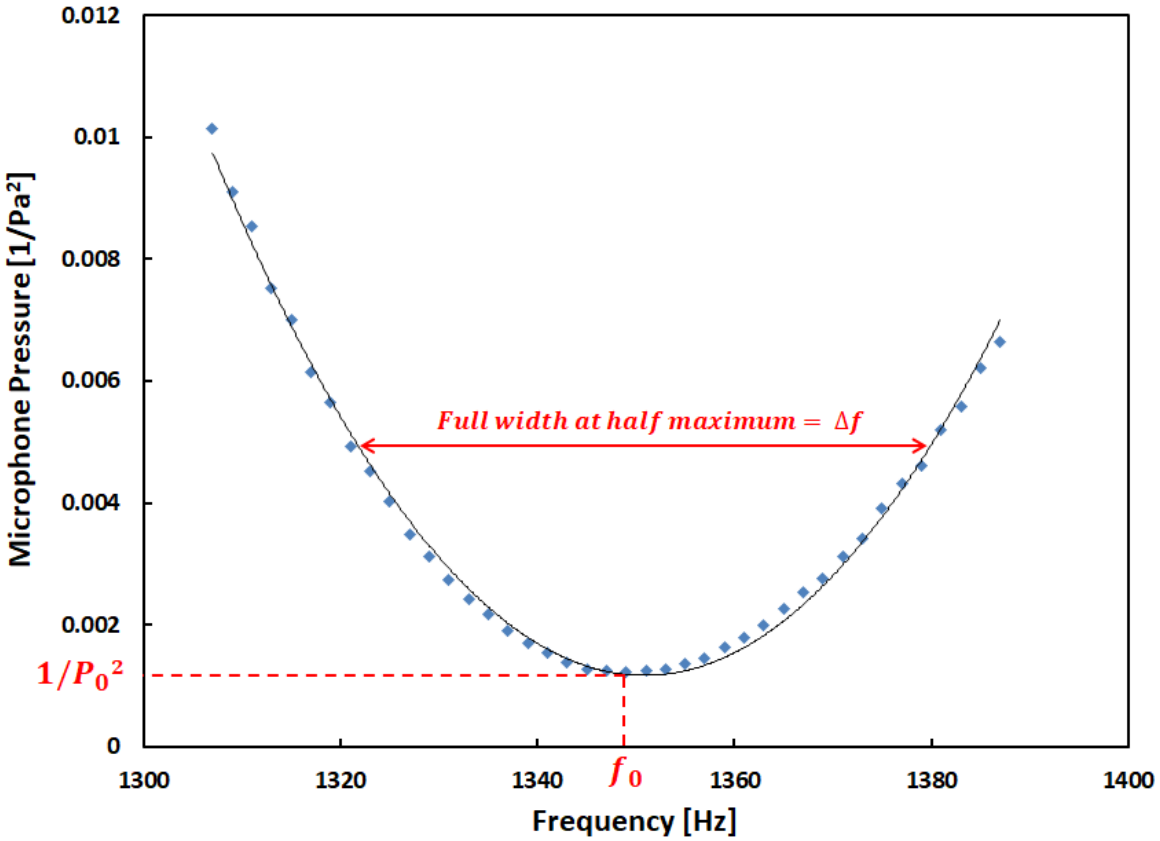

Figure 42. An example of the reciprocal of a resonance curve collected during acoustic calibration and the quadratic produced by the polynomial fit. The curve is used to determine the resonance frequency f_0, microphone pressure at resonance P_0, full width at half maximum Δf, and quality factor Q.

The microphone pressure values are inverted and squared to simplify the quadratic fit process. The Teensy performs the quadratic fit to these data using the following equations for Cramer's Rule to solve for three variables:

$$\begin{bmatrix} N & \sum X & \sum X^2 \\ \sum X & \sum X^2 & \sum X^3 \\ \sum X^2 & \sum X^3 & \sum X^4 \end{bmatrix} \begin{bmatrix} c \\ b \\ a \end{bmatrix} = \begin{bmatrix} \sum Y \\ \sum XY \\ \sum X^2 Y \end{bmatrix} , \quad (10)$$

$$a = \frac{\begin{vmatrix} N & \sum X & \sum Y \\ \sum X & \sum X^2 & \sum XY \\ \sum X^2 & \sum X^3 & \sum X^2 Y \end{vmatrix}}{\begin{vmatrix} N & \sum X & \sum X^2 \\ \sum X & \sum X^2 & \sum X^3 \\ \sum X^2 & \sum X^3 & \sum X^4 \end{vmatrix}} \; b = \frac{\begin{vmatrix} N & \sum Y & \sum X^2 \\ \sum X & \sum XY & \sum X^3 \\ \sum X^2 & \sum X^2 Y & \sum X^4 \end{vmatrix}}{\begin{vmatrix} N & \sum X & \sum X^2 \\ \sum X & \sum X^2 & \sum X^3 \\ \sum X^2 & \sum X^3 & \sum X^4 \end{vmatrix}} \; c = \frac{\begin{vmatrix} \sum Y & \sum X & \sum X^2 \\ \sum XY & \sum X^2 & \sum X^3 \\ \sum X^2 Y & \sum X^3 & \sum X^4 \end{vmatrix}}{\begin{vmatrix} N & \sum X & \sum X^2 \\ \sum X & \sum X^2 & \sum X^3 \\ \sum X^2 & \sum X^3 & \sum X^4 \end{vmatrix}} \quad . \quad (11)$$

Here, the matrices with square brackets denote regular matrices, while the matrices with vertical bars denote matrix determinants. X denotes the set of all frequency values that were

used in the quadratic fit, Y denotes the set of all pressure values used in the fit (inverted and squared), and N denotes the number of points in the data set. This quadratic fit yields the coefficients a, b, and c expressed as

$$y = ax^2 + bx + c \quad . \quad (12)$$

These coefficients are used to determine a more precise f_0, the microphone pressure at resonance P_0, and the quality factor Q of the resonator for the model in Eq. (9) and are given by

$$f_0 = \frac{-b}{2a} \quad , \quad (13)$$

$$P_0 = \sqrt{\frac{4a}{4ac-b^2}} \quad , \quad (14)$$

$$Q = \frac{f_0}{\Delta f} = \frac{|b|}{2} / \sqrt{4ac - |b|^2} \quad . \quad (15)$$

Once acoustic calibration is complete, the instrument begins background measurements. A pinch valve is activated, allowing filtered air to travel through the instrument's sample chamber.

The microphone pressure and laser power measured by the photodiode, as well as the f_0, P_0, and Q values acquired during acoustic calibration are used to calculate the absorption coefficient β_{abs} of the filtered air, known as the β_{abs} background. The simplified equation for β_{abs} is (Arnott et al. 1999)

$$\beta_{abs} = \frac{P_{mic}}{P_L}\frac{A_{res}\pi^2 f_0}{(\gamma-1)Q} . \quad (16)$$

More generally we subtract background signals, and select the microphone signal in phase with the laser beam modulation.

Background subtraction is implemented by sampling filtered air periodically. The expanded equations for the x and y components of β_{abs} that are used in the Teensy code to determine absorption background values are

$$\beta_{absxBG} = [\frac{A_{res}\pi^2 f_0}{(\gamma-1)Q}][\cos\varphi_0 (\frac{P_{micx}P_{laserx}+P_{micy}P_{lasery}}{{P_{laserx}}^2+{P_{lasery}}^2}) + \sin\varphi_0 (\frac{P_{micy}P_{laserx}-P_{micx}P_{lasery}}{{P_{laserx}}^2+{P_{lasery}}^2})] \quad (17)$$

$$\beta_{absyBG} = [\frac{A_{res}\pi^2 f_0}{(\gamma-1)Q}][-\sin\varphi_0 (\frac{P_{micx}P_{laserx}+P_{micy}P_{lasery}}{{P_{laserx}}^2+{P_{lasery}}^2}) + \cos\varphi_0 (\frac{P_{micy}P_{laserx}-P_{micx}P_{lasery}}{{P_{laserx}}^2+{P_{lasery}}^2})] \quad . (18)$$

In the above relationships, P_{mic}, P_{micx}, and P_{micy} denote the magnitude, the x component, and the y component of the microphone pressure; P_L, P_{laserx}, and P_{lasery} denote the magnitude, the x component, and the y component of the laser power measured with the photodiode; A_{res} denotes the cross-sectional area of the resonator; γ denotes the ratio of specific heats of air; and φ_0 denotes the phase offset which is calculated using the equation

R
E
F

R
e
f

$$P_L = \sqrt{{P_{laserx}}^2 + {P_{lasery}}^2} \quad , \quad (19)$$

$$\beta_{scaR} = \sqrt{{\beta_{scax}}^2 + {\beta_{scay}}^2} \quad , \quad (20)$$

$$\beta_{scaBG} = \left(\frac{\beta_{scaR}}{P_L}\right) \quad . \quad (21)$$

Here, P_{laserx}, P_{lasery}, β_{scax}, and β_{scay} denote the x and y components of the laser power and scattering signal recorded with the PJRC Audio Adaptor Board queues. These background measurements are taken to be the result of electrical noise within the system and will be subtracted from each main loop measurement. After these background measurements are taken, the pinch valve is deactivated in preparation for main loop measurements, and unfiltered air travels into the instrument.

Finally, main loop measurements are collected. Similar to the background measurement process, the instrument uses the microphone and photodiode signals to calculate β_{abs} and β_{sca} as shown in the following equations:

$$\beta_{absx} = \left[\frac{A_{res}\pi^2 f_0}{(\gamma-1)Q}\right]\left[\cos\varphi_0\left(\frac{P_{micx}P_{laserx}+P_{micy}P_{lasery}}{{P_{laserx}}^2+{P_{lasery}}^2}\right)+\sin\varphi_0\left(\frac{P_{micy}P_{laserx}-P_{micx}P_{lasery}}{{P_{laserx}}^2+{P_{lasery}}^2}\right)\right]-\beta_{absxBG} \quad , \quad (22)$$

$$\beta_{absy} = \left[\frac{A_{res}\pi^2 f_0}{(\gamma-1)Q}\right]\left[-\sin\varphi_0\left(\frac{P_{micx}P_{laserx}+P_{micy}P_{lasery}}{{P_{laserx}}^2+{P_{lasery}}^2}\right)+\cos\varphi_0\left(\frac{P_{micy}P_{laserx}-P_{micx}P_{lasery}}{{P_{laserx}}^2+{P_{lasery}}^2}\right)\right]-\beta_{absyBG} \quad , (23)$$

$$\beta_{sca} = \left(\frac{\beta_{scaR}}{P_L}\right) - \beta_{scaBG} \quad . \quad (24)$$

These measurements are outputted to an LCD screen. On-board sensors measure temperature, ambient pressure, and relative humidity inside and outside of the instrument plumbing during each β_{abs} and β_{sca} measurement.

Acoustic calibration and background measurements occur automatically after 400 measurements are conducted in the main loop. However, acoustic calibration and background measurements initiated sooner if internal temperature has changed significantly, or if the calibration button is pressed.

References

Abu-Rahmah, A., W. P. Arnott, and H. Moosmuller, 2006: Integrating nephelometer with a low truncation angle and an extended calibration scheme. *Measurement Science and Technology*, **17,** 1723-1732.

Aethlabs: Micro aethalometer. [Available online at https://aethlabs.com/microaeth/compare.]

Ajtai, T., A. Filep, G. Kecskemeti, B. Hopp, Z. Bozoki, and G. Szabo, 2011: Wavelength dependent mass-specific optical absorption coefficients of laser generated coal aerosols determined from

multi-wavelength photoacoustic measurements. *Applied Physics a-Materials Science & Processing*, **103,** 1165-1172.

Arnott, W. P., H. Moosmuller, C. F. Rogers, T. F. Jin, and R. Bruch, 1999: Photoacoustic spectrometer for measuring light absorption by aerosol: instrument description. *Atmospheric Environment*, **33,** 2845-2852.

Arnott, W. P., K. Hamasha, H. Moosmuller, P. J. Sheridan, and J. A. Ogren, 2005: Towards aerosol light-absorption measurements with a 7-wavelength Aethalometer: Evaluation with a photoacoustic instrument and 3-wavelength nephelometer. *Aerosol Science and Technology*, **39,** 17-29.

Arnott, W. P., I. J. Arnold, P. Mousset-Jones, K. Kins, and S. Shaff, 2008: R**eal-time Measurements of Diesel EC and TC in a Nevada Gold Mine With Photoacoustic and Dusttrak Instruments: Comparison With NIOSH 5040 Filter Results** *12th US/North American Mine Ventilation Symposium*.

Berkes, H., H. Jingnan, and R. Benincasa: An Epidemic Is Killing Thousands Of Coal Miners. Regulators Could Have Stopped It, 2018. [Available online at https://www.npr.org/2018/12/18/675253856/an-epidemic-is-killing-thousands-of-coal-miners-regulators-could-have-stopped-it.]

CDC: Mining Feature: Trend in Black Lung Cases Concerns NIOSH Researchers, 2011. [Available online at https://www.cdc.gov/niosh/mining/features/blacklung.html.]

Chen, D., X. W. Liu, J. K. Han, M. Jiang, Y. S. Xu, and M. H. Xu, 2018: Measurements of particulate matter concentration by the light scattering method: Optimization of the detection angle. *Fuel Processing Technology*, **179,** 124-134.

Consolino, L., F. Cappelli, M. S. de Cumis, and P. De Natale, 2019: QCL-based frequency metrology from the mid-infrared to the THz range: a review. *Nanophotonics*, **8,** 181-204.

Gillies, A. D. S., and H. W. Wu, 2006: Evaluation of a new real time personal dust meter for engineering studies. *11th US/North American Mine Ventilation Symposium*, Penn State Univ, University Pk, PA, Taylor & Francis Ltd, 167-+.

Halterman, A., S. Sousan, and T. M. Peters, 2018: Comparison of Respirable Mass Concentrations Measured by a Personal Dust Monitor and a Personal DataRAM to Gravimetric Measurements. *Annals of Work Exposures and Health*, **62,** 62-71.

Hofmann, W., 2011: Modelling inhaled particle deposition in the human lung-A review. *Journal of Aerosol Science*, **42,** 693-724.

Johann-Essex, V., C. Keles, M. Rezaee, M. Scaggs-Witte, and E. Sarver, 2017: Respirable coal mine dust characteristics in samples collected in central and northern Appalachia. *International Journal of Coal Geology*, **182,** 85-93.

Kosterev, A. A., F. K. Tittel, D. V. Serebryakov, A. L. Malinovsky, and I. V. Morozov, 2005: Applications of quartz tuning forks in spectroscopic gas sensing. *Review of Scientific Instruments*, **76,** 9.

Lebecki, K., M. Malachowski, and T. Soltysiak, 2016: Continuous Dust Monitoring in Headings in Underground Coal Mines. *Journal of Sustainable Mining*, **15,** 125-132.

Lewis, K., W. P. Arnott, H. Moosmuller, and C. E. Wold, 2008: Strong spectral variation of biomass smoke light absorption and single scattering albedo observed with a novel dual-wavelength photoacoustic instrument. *Journal of Geophysical Research-Atmospheres*, **113,** 14.

Maragkidou, A., O. Jaghbeir, K. Hameri, and T. Hussein, 2018: Aerosol particles (0.3-10 mu m) inside an educational workshop - Emission rate and inhaled deposited dose. *Building and Environment*, **140,** 80-89.

Marple, V. A., and K. L. Rubow, 1983: AN AEROSOL CHAMBER FOR INSTRUMENT EVALUATION AND CALIBRATION. *American Industrial Hygiene Association Journal*, **44,** 361-367.

Martonen, T. B., A. E. Barnett, and F. J. Miller, 1985: AMBIENT SULFATE AEROSOL DEPOSITION IN MAN - MODELING THE INFLUENCE OF HYGROSCOPICITY. *Environmental Health Perspectives*, **63,** 11-24.

McCartney, J. T., and S. Ergun, 1962: Refractive index and thickness of ultrathin sections of coals and graphite by interferometry. *Journal of the Optical Society of America*, **52,** 197-200.

Miller, A. L., A. T. Weakley, P. R. Griffiths, E. G. Cauda, and S. Bayman, 2017: Direct-on-Filter alpha-Quartz Estimation in Respirable Coal Mine Dust Using Transmission Fourier Transform Infrared Spectrometry and Partial Least Squares Regression. *Applied Spectroscopy*, **71,** 1014-1024.

Mischler, S. E., D. P. Tuchman, E. G. Cauda, J. F. Colinet, and E. N. Rubinstein, 2019: Testing a revised inlet for the personal dust monitor. *Journal of occupational and environmental hygiene*, 1-8.

Moosmuller, H., and Coauthors, 2001a: Time-resolved characterization of diesel particulate emissions. 2. Instruments for elemental and organic carbon measurements. *Environmental Science & Technology*, **35,** 1935-1942.

——, 2001b: Time resolved characterization of diesel particulate emissions. 1. Instruments for particle mass measurements. *Environmental Science & Technology*, **35,** 781-787.

Moosmüller, H., R. K. Chakrabarty, and W. P. Arnott, 2009: Aerosol Light Absorption and its Measurement: A Review. *Journal of Quantitative Spectroscopy & Radiative Transfer*, **110,** 844-878.

MSHA: Respirable Dust Rule: A Historic Step Forward in the Effort to End Black Lung Disease, 2016. [Available online at https://www.msha.gov/news-media/special-initiatives/2016/09/28/respirable-dust-rule-historic-step-forward-effort-end.]

NASEM: To Increase Protection of Miners from Black Lung Disease, A Comprehensive Report

on Underground Coal Mine Dust Exposure Says Monitoring and Sampling Should Go

Beyond Regulatory Compliance, 2018. [Available online at http://www8.nationalacademies.org/onpinews/newsitem.aspx?RecordID=25111.]

Noll, J., S. Janisko, and S. E. Mischler, 2013: Real-time diesel particulate monitor for underground mines. *Analytical Methods*, **5,** 2954-2963.

Patashnick, H., and E. G. Rupprecht, 1991: CONTINUOUS PM-10 MEASUREMENTS USING THE TAPERED ELEMENT OSCILLATING MICROBALANCE. *Journal of the Air & Waste Management Association*, **41,** 1079-1083.

ThermoScientific, 2019a: Personal Dust Monitor.

——, 2019b: Thermo Scientific Scientific Personal DataRam pDR-1500 Monitor.

TSI: Optical Particle Sizer Model 3330. [Available online at https://www.tsi.com/optical-particle-sizer-3330/.]

8.0 Acknowledgement/Disclaimer

This study was sponsored by the Alpha Foundation for the Improvement of Mine Safety and Health, Inc. (ALPHA FOUNDATION). The views, opinions and recommendations expressed herein are solely those of the authors and do not imply any endorsement by the ALPHA FOUNDATION, its Directors and staff. We gratefully acknowledge the NIOSH team lead by Dr. Jay F. Colinet for expertly directing the field campaign, held at the Pittsburgh NIOSH laboratory, for testing the prototype instrument.